# Non-orographic gravity waves and turbulence caused by merging jet streams

Wolfgang Woiwode[1], Andreas Dörnbrack[2], Markus Geldenhuys[3], Felix Friedl-Vallon[1], Andreas Giez[4], Thomas Gulde[1], Michael Höpfner[1], Soeren Johansson[5], Bernd Kaifler[6], Anne Kleinert[1], Lukas Krasauskas[3], Erik Kretschmer[1], Guido Maucher[1], Tom Neubert[7], Hans Nordmeyer[1], Christof Piesch[1], Peter Preusse[8], Markus Rapp[9], Martin Riese[10], Ulrich Schumann[11], and Jörn Ungermann[12]

[1]Institute of Meteorology and Climate Research, Karlsruhe Institute of Technology (KIT)
[2]DLR, Institut für Physik der Atmosphäre
[3]Institute of Energy and Climate Research (IEK-7: Stratosphere), Forschungszentrum Jülich
[4]Deutsches Zentrum für Luft- und Raumfahrt
[5]Karlsruhe Institute of Technology
[6]Institute of Atmospheric Physics, German Aerospace Center
[7]Zentralinstitut für Engineering, Elektronik und Analytik-Systeme der Elektronik (ZEA-2), Forschungszentrum Jülich (FZJ)
[8]Juelich Research Center
[9]Deutsches Zentrum für Luft- und Raumfahrt (DLR)
[10]Forschungszentrum Juelich
[11]DLR
[12]Institute of Energy and Climate Research - Stratosphere (IEK-7), Research Centre Jülich

December 7, 2022



**Abstract**

Jet streams are important sources of non-orographic internal gravity waves and clear air turbulence (CAT). We analyze non-orographic gravity waves and CAT during a merging of the polar front jet stream (PFJ) with the subtropical jet stream (STJ) above the southern Atlantic. Thereby, we use a novel combination of airborne observations covering the meso-scale and turbulent scale in combination with high-resolution deterministic short-term forecasts. Coherent phase fronts stretching along a highly sheared tropopause fold are found in the ECMWF IFS (integrated forecast system) forecasts. During the merging event, the PFJ reverses its direction from antiparallel to parallel with respect to the STJ, going along with strong wind shear and horizontal deformation. Temperature perturbations in limb-imaging and lidar observations onboard the research aircraft HALO in the framework of the SouthTRAC campaign show remarkable agreement with the IFS data. Ten hours earlier, the IFS data show a new "X-shaped" phase line pattern emanating from the sheared tropopause fold. The analysis of tendencies in the IFS wind components shows that these gravity waves are excited by a local body force as the PFJ impinges the STJ. In situ observations of temperature and wind components at 100 Hz confirm upward propagation of the probed portion of the gravity waves. They furthermore reveal embedded episodes of light-to-moderate CAT, Kelvin Helmholtz waves, and indications for partial wave reflection. Patches of low gradient Richardson numbers in the IFS data coincide with episodes where CAT was observed, suggesting that this event was well accessible to turbulence forecasting.

# Non-orographic gravity waves and turbulence caused by merging jet streams

**W. Woiwode[1], A. Dörnbrack[2], M. Geldenhuys[3], F. Friedl-Vallon[1], A. Giez[4], T. Gulde[1], M. Höpfner[1], S. Johansson[1], B. Kaifler[2], A. Kleinert[1], L. Krasauskas[3], E. Kretschmer[1], G. Maucher[1], T. Neubert[5], H. Nordmeyer[1], C. Piesch[1], P. Preusse[3], M. Rapp[2,6], M. Riese[3], U. Schumann[2] and J. Ungermann[3]**

[1]Institute of Meteorology and Climate Research, Karlsruhe Institute of Technology (KIT), Karlsruhe, Germany

[2]Deutsches Zentrum für Luft- und Raumfahrt, Institut für Physik der Atmosphäre (DLR-IPA), Oberpfaffenhofen, Germany

[3]Institute of Energy and Climate Research – Stratosphere (IEK-7), Forschungszentrum Jülich (FZJ), Jülich, Germany

[4]Deutsches Zentrum für Luft- und Raumfahrt, Einrichtung Flugexperimente (DLR-FX), Oberpfaffenhofen, Germany

[5]Zentralinstitut für Engineering, Elektronik und Analytik-Systeme der Elektronik (ZEA-2), Forschungszentrum Jülich (FZJ), Jülich, Germany

[6]Meteorologisches Institut München, Ludwig-Maximilians-Universität München, Munich, Germany

Corresponding author: Wolfgang Woiwode (wolfgang.woiwode@kit.edu)

**Key Points:**

- Non-orographic internal gravity waves and clear air turbulence are observed in merging jet streams
- State-of-the art high resolution forecast agrees with novel combination of airborne sensors
- A new “X-shaped” gravity wave structure that emenanates from a sheared tropopause fold is analysed

## Abstract

Jet streams are important sources of non-orographic internal gravity waves and clear air turbulence (CAT). We analyze non-orographic gravity waves and CAT during a merging of the polar front jet stream (PFJ) with the subtropical jet stream (STJ) above the southern Atlantic. Thereby, we use a novel combination of airborne observations covering the meso-scale and turbulent scale in combination with high-resolution deterministic short-term forecasts. Coherent phase fronts stretching along a highly sheared tropopause fold are found in the ECMWF IFS (integrated forecast system) forecasts. During the merging event, the PFJ reverses its direction from antiparallel to parallel with respect to the STJ, going along with strong wind shear and horizontal deformation. Temperature perturbations in limb-imaging and lidar observations onboard the research aircraft HALO in the framework of the SouthTRAC campaign show remarkable agreement with the IFS data. Ten hours earlier, the IFS data show a new "X-shaped" phase line pattern emanating from the sheared tropopause fold. The analysis of tendencies in the IFS wind components shows that these gravity waves are excited by a local body force as the PFJ impinges the STJ. In situ observations of temperature and wind components at 100 Hz confirm upward propagation of the probed portion of the gravity waves. They furthermore reveal embedded episodes of light-to-moderate CAT, Kelvin Helmholtz waves, and indications for partial wave reflection. Patches of low gradient Richardson numbers in the IFS data coincide with episodes where CAT was observed, suggesting that this event was well accessible to turbulence forecasting.



## Plain Language Summary

Gravity waves play an in important role in vertical and horizontal energy transport in the atmosphere and are significant factors in wheather forecasting and climate projections. Among other processes, tropopsheric jet streams are known to be sources of gravity waves. They furthermore can be accompanied by tropopause folds (i.e. local tropopause depressions, where stratospheric air can reach deeply into the troposphere) and turbulence, which is relevant for aviation safety. Using a novel combination of airborne observations and data by a state-of-the-art forecasting system, we analyse gravity waves and turbulence during a merger of tropospheric jet streams above the southern Atlantic. The observations show a high degree of agreement with the forecast data from the troposphere to the stratosphere. Ten hours earlier, the forcast data show a new "X-shaped" gravity wave structure that emerges from a highly sheared tropopause fold between the merging jet streams. Fast in situ observations at the flight level provide information on the characteristics of the observed waves and show light-to-moderate turbulence, small-scale waves and indications for partial wave reflection. The observed turbulence events are located in regions where the forecast data consistently show conditions that are supportive for turbulence.


## 1 Introduction

Jet streams and fronts are important sources of non-orographic gravity waves. Their complex generation mechanisms are subject of ongoing research (Plougonoven and Zhang, 2014). Non-orographic gravity waves have been shown to contribute to the vertical momentum flux in a manner comparable to orographic sources (Hertzog et al., 2008; Plougonoven et al., 2013; Dörnbrack et al., 2022). Different excitation mechanisms, often occurring within geostrophic adjustment processes (e.g. O'Sullivan and Dunkerton, 1995), are reported in literature and include, amongst other mechanisms, transient generation by sheared disturbances and shear instabilities on small scale (Plougonoven and Zhang, 2014, and references therein) as well as the stratospheric flow across propagating Rossby wave trains (Dörnbrack et al. 2022). Correlation analyses based

on intensive radiosonde observations above Wuhan and Yichang, China, have shown that the vertical shear of the horizontal wind at the tropospheric jet is an important source of non-orographic gravity waves in the troposphere and stratosphere (Zhang and Yi, 2005, 2008).

Clear air turbulence (CAT) occurs in the vicinity of tropospheric jet streams and represents an important mechanism for mass exchange between the stratosphere and the troposphere (Shapiro, 1980; Gettelmann et al., 2011, and references therein). CAT is of high relevance to global aviation safety (Kennedy and Shapiro, 1975; Sharman et al., 2012, and references therein). Gravity waves generated by jets and fronts can be sources of CAT, since they are accompanied by vertical shear and discontinuities in static stability in the tropopause region (Knox 1997; Koch et al. 2005; Knox et al., 2008, Plougonoven et al., 2016, and references therein). Furthermore, they are able to modify the ambient shear and stability in such a way that instabilities leading to CAT are more easily triggered, a process already mentioned by Panofsky et al. (1968). Thus, it is important to analyse observations of non-orographic gravity waves and CAT associated with tropospheric jet streams and to test whether the associated mechanisms of wave excitation and their effects on conditions supportive to CAT are represented by state-of-the-art forecasting systems.

Non-orographic gravity waves and turbulence in the vicinity of jet streams are difficult to access observationally, since their generation and propagation occurs under non-stationary and transient conditions, often at remote locations (e.g., above oceans) on the globe (Rodriguez Imazio et al., 2022). The standard observational systems that are capable of resolving non-orographic gravity waves on mesoscale and turbulent scale are scarce and observations are mainly limited to selected radiosonde profiles (e.g. Plougonven & Teitelbaum, 2003; Dörnbrack et al., 2018), or to aircraft observations. In the framework of the SouthTRAC mission from September to November 2019, the SouthTRAC-GW (Southern hemisphere Transport, Dynamics, and Chemistry - Gravity Waves) campaign was conducted to probe gravity waves in the hotspot region around the southern part of South America and the Antarctic peninsula (Rapp et al., 2021). Among other objectives, goals of SouthTRAC-GW were to provide detailed measurements of orographic and non-orographic gravity waves for comparisons with high-resolution simulations, to explore breaking and dissipation of gravity waves, and to compare the identification of gravity waves seen by different measurement techniques. During SouthTRAC, the combination of airborne limb-imaging observations below the aircraft by GLORIA (Gimballed Limb Observer for Radiance Imaging of the Atmosphere; Friedl-Vallon et al., 2014; Riese et al., 2014), with ALIMA (Airborne LIdar for Middle Atmosphere research; Rapp et al., 2021) above the aircraft and BAHAMAS (Basic Halo Measurement and Sensor System; Krautstrunk & Giez, 2012; Giez et al., 2017, 2019, 2021) at the flight level was available onboard the German research aircraft HALO (High Altitude and LOng Range Research Aircraft) for the first time. These observations allowed focused observations of gravity waves from the troposphere to the mesosphere and on the meso-scale and turbulent scale.

The stratospheric polar vortex during austral winter is usually stable, i.e. less affected by planetary waves as its northern hemispheric counterpart, and it lasts long into spring. However, in September 2019, the rare event of a minor sudden stratospheric warming (SSW) in the southern hemisphere occurred after a poleward shift of the polar night jet stream (Dörnbrack et al., 2020; Lim et al., 2021). The mean Antarctic warming in the midstratosphere during spring 2019 resulted in a new record, while the deceleration of the vortex was comparable with the first-ever observed sudden stratospheric warming on the southern hemisphere in 2002. In the austral winter 2019, tropospheric weather systems were often affected by blocking of the airflow above the Pacific upstream of the southern Andes. This resulted in a less distinct separation of the polar front jet (PFJ) and the

subtropical jet stream (STJ) (S. Knobloch, personal communication, 2022) and situations where the PFJ approached the STJ under steep angles in the horizontal domain such as analysed here.

In this study, we analyze non-orographic gravity waves caused by merging jet streams over the Atlantic Ocean far from the South American landmass. These gravity waves were predicted in advance by the ECMWF (European Centre for Medium-Range Weather Forecasts) Integrated Forecast System (IFS) as they were generated during a merger of the PFJ with the STJ that lead to a strongly deformed horizontal airflow. The scenario is analyzed with the help of ECMWF IFS high-resolution short-term forecasts and operational analyses, as well as dedicated airborne observations by GLORIA, ALIMA and BAHAMAS onboard HALO during the SouthTRAC research flight ST10 on 16-17 September 2019. Thereby, the following research questions are addressed:

- Do the location and the amplitudes of the predicted non-orographic gravity waves in the IFS data agree with the airborne observations?
- Where is the origin of these gravity waves and how are they excited?
- Are there indications of small-scale waves and CAT, and how are they affected by these non-orographic gravity waves?

As mentioned earlier, the observations were made for an event where the PFJ and STJ merge over the southern Atlantic, a remote region usually not covered by high-resolution observations. That is why we are anticipating new insights into another possible scenario of CAT generation in connection with non-orographic gravity waves.

In Section 2, the observations, model data and methods used for data analysis are introduced. The overall meteorological situation during ST10 and the jet stream merging event is discussed in Section 3. A detailed analysis of the jet stream merging event and the non-orographic gravity waves based on the IFS data and the observations is presented in Section 4. Using the IFS and trajectories, we investigate the temporal evolution and the origin of the observed waves and turbulence. In Section 5, we discuss our results and conclude the paper.

## 2 Data and Methods

To study the meteorological situation and non-orographic gravity waves above the southern Atlantic on 16-17 September 2019, we use ECMWF IFS and ERA5 data together with the combination of the instruments GLORIA, ALIMA and BAHAMAS that was deployed onboard HALO during SouthTRAC for the first time (Figure 1).

### 2.1 GLORIA limb-imaging observations

GLORIA (Gimballed Limb Observer for Radiance Imaging of the Atmosphere) is an infrared limb-imager that has been developed for high-altitude aircraft and stratospheric balloons (Friedl-Vallon et al., 2014; Riese et al. 2014). In the configuration applied during SouthTRAC, 128 vertical times 48 horizontal pixels of the GLORIA detector array were used for simultaneous limb-imaging observations from ~5 km up to the flight altitude (typically 12 to 13 km). Since each pixel records an interferogram, the observations represent data cubes. The interferograms are transformed into spectra, and the spectra associated with one detector row within a data cube are binned, thus resulting in 128 spectra with different limb viewing angles per data cube. The spectral range from 780 to 1400 $cm^{-1}$ covered by GLORIA includes spectral signatures of many trace gases (e.g. $CO_2$, $O_3$, $H_2O$, chlorofluorocarbons, and pollution gases) and aerosols. The performance and

processing of the GLORIA measurements have been improved continuously over the last years. The GLORIA observations during SouthTRAC are characterized by instrumental gain and offset errors as low as 1 % and 30 nW $cm^{-2}$ $sr^{-1}$ cm, respectively (Ungermann et al., 2022). From the GLORIA observations, vertical profiles and 3D distributions of temperature, trace gas volume mixing ratios, and clouds are retrieved (e.g. Krisch et al., 2017; Johansson et al., 2018; Krasauskas et al., 2021; Wetzel et al., 2022).

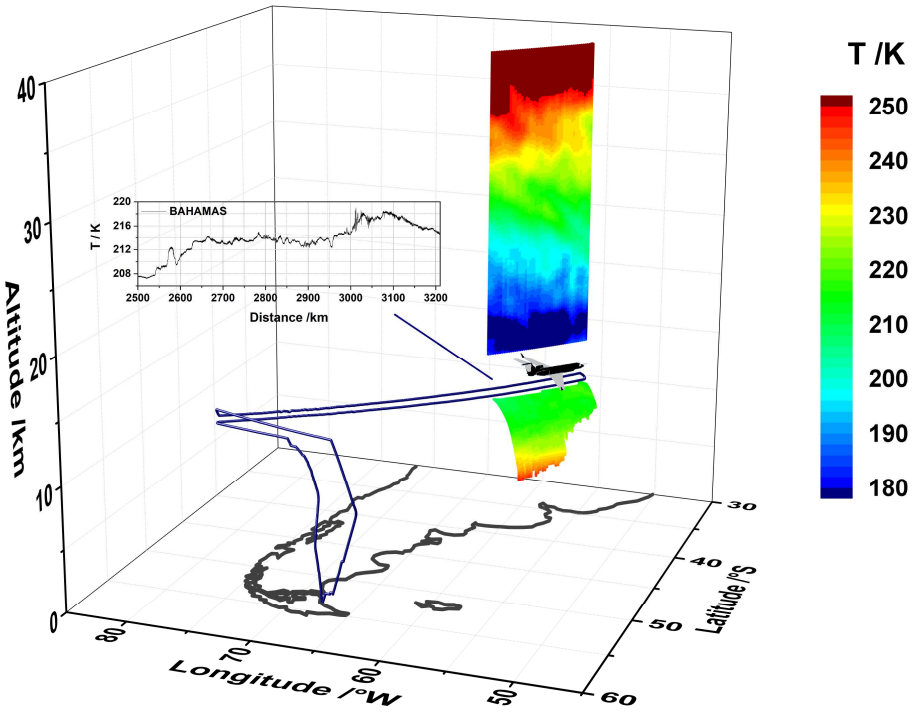


**Figure 1.** Remote sensing and in situ observations onboard HALO to study gravity waves. Temperature measurements by the GLORIA infrared limb-imager are shown underneath and to the south-east, those from the upward-looking ALIMA lidar are shown directly above the flight track, and BAHAMAS in situ data are displayed schematically in the background for the portion of HALO research flight ST10 examined here.

GLORIA can be operated in different measurement modes that include different spectral resolution and sampling. Here, we use GLORIA observations in the "chemistry mode", which involves a high spectral sampling of 0.0625 $cm^{-1}$ in combination with a fixed azimuth orientation (i.e. no tomographic sampling by means of azimuth panning), resulting in one data cube of GLORIA observations and thereby one vertical profile of each target parameter within ~3 km horizontal flight distance (Johansson et al., 2018). In particular, we use GLORIA temperature (water vapor) profiles, which are characterized by a combined random and systematic error of ~1 K (~15 %) and a typical vertical resolution of <500 m (<400 m), respectively. The vertical profiles characterize the atmospheric scenario near the tangent points of the GLORIA limb observations, which are located on the right side of the HALO flight track. For each parameter, the individual vertical profiles retrieved from the GLORIA observations are combined to vertical cross-sections along the HALO flight track. Note that the tangent points of the upper limb observations are

situated close to the flight level, while they are farther away in horizontal direction for lower viewing angles (see Fig. 1). Thus, the vertical cross-sections obtained from GLORIA do not reflect the situation below the flight track (i.e. normal to the earth surface), but are located on a curved surface projected by the GLORIA tangent points along the flight path (see Fig. 1). This property is accounted for in the following model comparisons by interpolating the IFS data to the GLORIA tangent points instead of normal to the flight path.

### 2.2 ALIMA lidar observations

ALIMA (Airborne Lidar for Middle Atmosphere research) is an upward pointing Rayleigh lidar which uses an Nd:YAG laser operating at 532 nm wavelength (Rapp et al., 2021). Using three height-cascaded elastic detector channels, atmospheric density profiles from a few kilometers above flight altitude up to 90 km are measured and are converted to temperature profiles by hydrostatic integration in a similar way as with data acquired by ground-based lidar instruments (Kaifler and Kaifler, 2021). For ST10, from 20 to 35 km the corresponding mean absolute error is approximately constant at 1.4 K, since the signal is distributed over the three height-cascaded detector channels, and increases to 5.3 K at 50 km. Below 20 km, absolute errors are larger than 1.4 K. However, relative temperature perturbations induced by gravity waves can still be derived accurately by de-trending the data by means of a horizontal mean, thus making the analysis less sensitive to systematic uncertainties (Ehard et al., 2015). The individual ALIMA profiles are combined to form vertical cross-sections above the HALO flight track in the upright direction. Here, we use ALIMA temperature data with 5 min temporal and 1500 m vertical resolution.

### 2.3 BAHAMAS in situ observations

BAHAMAS is the Basic HALO Measurement and Sensor System of HALO (Krautstrunk & Giez, 2012). BAHAMAS consists of a nose boom probe with a 5-hole sensor and provides in situ measurements of horizontal and vertical wind components as well as temperatures, pressures, and water vapor mixing ratios at flight altitude with high temporal resolution, i.e. up to 100 Hz (Giez et al., 2017, 2019). Giez et al. (2021) presented a detailed and complete description of the different calibration steps of the BAHAMAS sensor for the German research aircraft HALO. Here, we use BAHAMAS measurements of static air temperature and the three wind components u, v, and w. The standard BAHAMAS data products are available with a temporal resolution of 1 and 10 Hz. High temporal 100 Hz resolution can be achieved after a dedicated post processing, which was conducted for the flight section analyzed here. Appendix B of Dörnbrack et al. (2022) contains a comparison of the SouthTRAC spectra from all available 10 Hz and 100 Hz data. The spectra of the 10 Hz and 100 Hz velocity components are very similar in the 0.4 to 4 Hz analysis interval applied to determine the energy dissipation rates used in this study, a result that promotes confidence in the well-calibrated BAHAMAS measurements (Giez et al., 2021). According to Krautstrunk & Giez (2014) and Giez et al. (2017, 2019, and personal communication), the static air temperature data is characterized by absolute errors ($1\sigma$) of 0.3 K and the static air pressure data by 0.2 hPa. The absolute errors ($1\sigma$) of the horizontal and vertical wind components u, v, and w are 0.3 m $s^{-1}$, 0.5 m $s^{-1}$, and 0.6 m $s^{-1}$, respectively.

### 2.4 ECMWF IFS and ERA5 data

The IFS is the state-of-the-art global numerical weather prediction system operational at the ECMWF. Here, we use high-resolution 1-hourly deterministic short-term forecasts and six-hourly operational analyses by the IFS (Hólm et al., 2016; Malardel & Wedi, 2016) to analyze the synoptic and mesoscale scenario and its temporal evolution. The IFS forecast and analysis data is computed on a cubic octahedral grid at a spectral truncation of 1279, which corresponds to a horizontal resolution of ~9 km and is interpolated to a regular 0.25° x 0.25° latitude-longitude grid. The data include 137 vertical levels, from the ground up to the model top at ~0.01 hPa, and have a vertical resolution of ~400 m in the tropopause region. In particular, we use IFS temperature, pressure, wind, potential vorticity, and specific humidity ($q_v$) data to investigate the evolution of the atmospheric scenario during SouthTRAC research flight ST10.

For the meteorological flight overview in Section 3, we furthermore show ECMWF ERA5 data (Hersbach et al., 2020). The data are available at 137 levels from the surface to ~80 km and provide hourly estimates of atmospheric variables at a slightly coarser horizontal resolution (~30 km) than the operational IFS products.

### 2.5 Data analysis

#### 2.5.1 IFS fields and comparison with observations

We use vertical and horizontal cross sections of the IFS fields to analyze the meteorological situation, gravity waves, and the temporal evolution of the atmospheric variables along the flight track of ST10. For this purpose, the spatially interpolated IFS data are shown at the indicated model time steps without interpolation in time. In the direct comparisons with the observations by GLORIA, ALIMA and BAHAMAS, the IFS data are interpolated linearly in time and space to the measurement geolocations. For comparisons with the BAHAMAS turbulence data in the vicinity of the flight track (see Fig. 9), the IFS data were interpolated to a regular vertical 500 m grid along the flight track. From the interpolated data, the squared Brunt–Väisälä frequency

$$N^2 = \frac{g}{\theta}\frac{d\theta}{dz} \quad (1)$$

and the squared vertical shear of the horizontal wind speed

$$S^2 = \left(\frac{du}{dz}\right)^2 + \left(\frac{dv}{dz}\right)^2 \quad (2)$$

were calculated with the potential temperature $\Theta$, the altitude z, and and the zonal and meridional wind components u and v. The gradient Richardson number (Ri) is the quotient of $N^2$ and $S^2$ (see Mauritsen and Svensson, 2007, and references therein).

The GLORIA chemistry mode data feature dense horizontal sampling along flight track (~3 km) and high vertical resolutions (< 500 m), thus providing a resolved picture of the atmospheric scenario *along* flight track. However, limb observations without tomographic sampling are characterized by a low horizontal resolution along their line of sight (here: *across* flight track, i.e. along viewing direction), which is given by the width of weighting function of the radiative transfer. It varies from a several tens of kilometers (near flight altitude) to a few hundreds

of kilometers (at the lowest tangent points). This effect can be accounted for by a more complex model interpolation involving observational filters (Ungermann et al., 2011). However, for comparisons with the GLORIA limb observations shown here, the IFS data are interpolated to the tangent point geolocations of the GLORIA observations without considering an observational filter. This approach is suitable here, since the flight section of research flight ST10 was planned and flown in a way such that strong horizontal gradients of atmospheric variables along the line of sight were avoided. Thus, the dense horizontal sampling *along* flight track was exploited to resolve the atmospheric variations of interest, while the instrument's line of sight was aligned into directions with low variations in the atmospheric quantities.

To account for the limited grid spacing (0.25° x 0.25°) of the representation of the IFS data used here, as well as knowing the large-scale nature of the targeted gravity waves, the GLORIA and ALIMA profiles are furthermore subjected each to a moving ~50 km horizontal mean in the comparisons of the vertical cross sections.

### 2.5.2 Temperature perturbations by gravity waves

To identify temperature perturbations $\Delta T$ due to gravity waves in the IFS data, we de-trended the IFS temperature data by subtracting spectrally truncated data with T106 resolution from the fully resolved IFS fields on the same grid. The reader is referred to Gupta et al. (2021) or Dörnbrack (2021) for similar applications of this method. For direct comparisons with the observations, a different approach was applied for an independent, self-consistent de-trending of each the GLORIA, ALIMA and IFS data. In this case, we calculated for each data set the mean temperature profile of the ~700 km (~45 min) flight section that is in the focus here. Then, for each data set, the corresponding mean temperature profile was subtracted from the individual temperature profiles along this flight section.

### 2.5.3 Trajectories

To investigate the flow during the evolution of the observed gravity waves, trajectories were calculated with the Hybrid Single-Particle Lagrangian Integrated Trajectory model (HYSPLIT) by NOAA's (National Oceanic and Atmospheric Administration) Air Resources Laboratory (Draxler and Hess, 1998; Stein et al., 2015 and references therein). In particular, we used the HYSPLIT-WEB online tool (https://www.ready.noaa.gov/HYSPLIT.php, last access: July 5, 2022) to calculate isentropic backward trajectories based on NOAA's archived Global Forecast System (GFS) 3-hourly forecast data at 0.25° x 0.25° resolution. Although not identical with the IFS data used in the other analyses, the GFS data are acceptable for our purpose, since both model systems are well-proven, involve a similar dynamical core (e.g. Magnusson et al., 2019), and short lead times of less than one day are considered.

### 2.5.4 Turbulence observations

To quantify the CAT encountered during the flight section analyzed here, the cube root of the energy dissipation rate $\varepsilon$ was calculated according to Bramberger et al., (2018, 2020). As discussed by these authors, this parameter is referred to as EDR and can be used to estimate the aircraft response according to the ICAO (International Civil Aviation Organization) categories for "light", "moderate", "severe" and "extreme" CAT (ICAO 2001, Sharman et al., 2014). Thereby, EDR is calculated by the inertial dissipation technique and assuming the Kolmogorov form of the turbulent energy spectrum (e.g., Strauss et al., 2015). Using this approach, EDR values are

available for each of the components of the wind vector. Estimates of the energy dissipation rates computed from the 10 Hz as well as 100 Hz BAHAMAS data are available for the whole SouthTRAC research flights, see Dörnbrack et al. (2022). Furthermore, wave energy flux, momentum flux and energy densities are calculated according to Dörnbrack et al. (2022).

## 3 Meteorological situation and flight overview

The austral winter 2019 was characterized by the earliest observed SSW in the southern hemisphere (Dörnbrack et al., 2020; Lim et al., 2021; Rapp et al., 2021). In August 2019, the center of the stratospheric polar vortex shifted away from the pole and its shape elongated, which was followed by the minor SSW in September 2019. A consequence of the northwards displacement was that the cold polar vortex was moved above southern Argentina and Chile. This resulted in the unusual event of mother-of-pearl clouds above El Calafate, Argentina at 50°21′S that were observed visually from ground and the Perlan 2 aircraft (Dörnbrack et al, 2020). In early September 2019, zonal winds in the upper stratosphere considerably weakened, thus generating a critical level for stationary mountain waves that confined their vertical propagation to altitudes lower than 40 km. At the same time, a blocking anticyclone above the Pacific resulted in weather systems with tropospheric jet streams approaching the southern Andes frequently in eastern to north-eastern directions, and a less clear separation of the southern PFJ and STJ when compared to other austral winters.

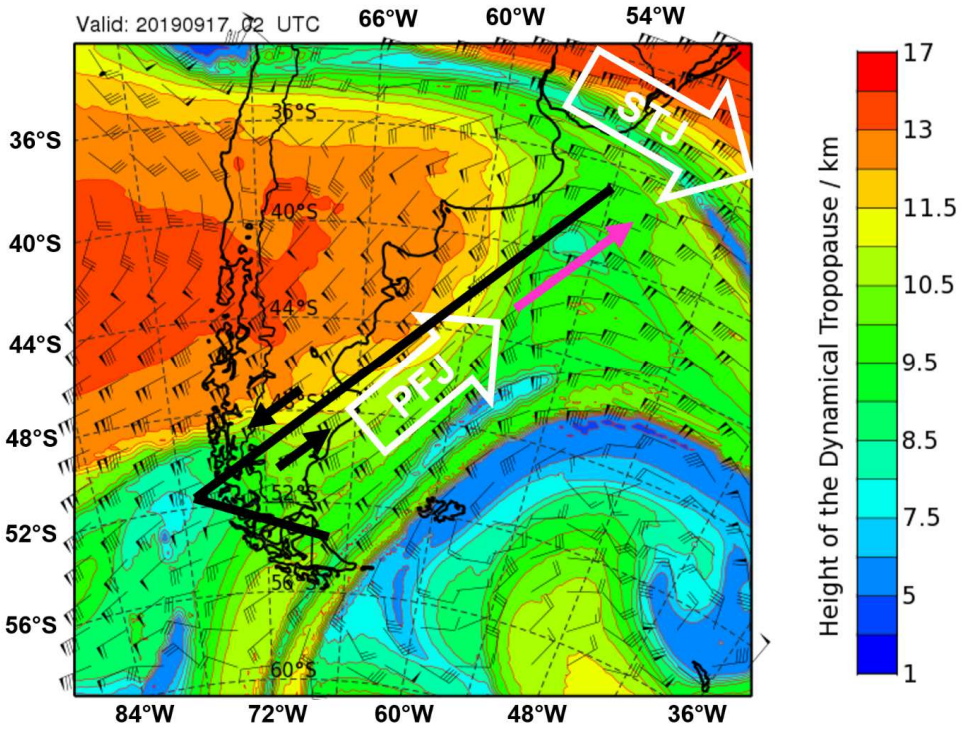


**Figure 2.** Upper-level atmospheric airflow during the merging event of the polar front jet (PFJ) and the subtropical jet (STJ) valid on 17 September 2019 02 UTC. Height of the dynamical tropopause (km, color-shaded) and horizontal wind at the dynamical tropopause (short barbs 5 m $s^{-1}$, long barbs 10 m $s^{-1}$, triangles 50 m $s^{-1}$) from ECMWF ERA5 reanalysis. The HALO flight track is indicated schematically by a black line. Magenta arrow: focus region of this study.

SouthTRAC research flight ST10 was conducted on 16 and 17 September 2019, during the SSW. Figure 2 shows the upper-level airflow by means of the height of the dynamical tropopause and the associated horizontal winds by a synoptic map corresponding to the time of the middle of the flight track. A strong ridge is seen in Figure 2 above the Pacific, Chile and the northern part of Argentina. A mature low-pressure system is located above the Atlantic, east of the Drake Passage with its core north of South Georgia. North of 36°S, a strong STJ is seen that is accompanied by an elongated tropopause fold south of it. Between the ridge and the low, the PFJ is aligned in a southwesterly direction across northern Patagonia and above the Atlantic. In the focus region of this study (magenta arrow in Figure 2), the PFJ has a strong cyclonic curvature and merges with the STJ over the Atlantic. A narrow intrusion associated with the PFJ is seen at ~39°S/55°W.

The flight track of HALO is plotted schematically in Figure 2. HALO took off in Rio Grande at Tierra del Fuego on 16 September 2019 at 23:00 UTC and crossed the Southern Andes towards the Pacific. After a turn to the northeast, the Andes were crossed again, and HALO flew a long leg across Patagonia and the Atlantic with a northeasterly heading. The outermost waypoint at 36.8°S/54.1°W was reached on 17 September 2019 at 02:40 UTC. Here, HALO turned around and followed the same flight path back to Rio Grande, where it landed at 07:44 UTC.

# 4 Results

## 4.1 Synoptic situation and gravity waves in IFS data

Figure 3a and 3b show the horizontal wind field approximately at flight altitude and along the vertical cross-section of the flight path which is indicated in Figure 3a. Similar to the upper-level airflow shown in Figure 2, the STJ is located in the north-east of the panel, and the PFJ extends from the southern Andes and Patagonia towards the Atlantic, where it merges with the STJ (Fig. 3a). In the vertical cross section, the STJ and PFJ are situated at the dynamical tropopause. Here, the polar night jet (PNJ) at about 35 km altitude is located between about 50°W and 65°W which corresponds to low geographic latitudes of about 40°S due to the equatorward shift of the stratospheric polar vortex during the SSW.

At the STJ, a distorted tropopause fold with stratospheric air intruding into the troposphere is seen in Figure 3b. West of the tropopause fold the weak intrusion is seen in the vertical cross section (57°W, compare Fig. 2), which was reached by HALO in the outermost section of the flight ("focus region", blue box). While the STJ and PFJ reach maximum wind speeds larger than 70 m/s in their core regions, moderate wind speeds of around 50 m/s are found in their merging zone. Within and around the focus region, slanted patches of lower wind speeds less than 40 m/s are found above the tropopause indicating layers of enhanced horizontal wind shear. They coincide with regions where a steepening of isentropic surfaces is seen between the tropopause and the PNJ in Figure 3b.

Figures 3c and 3d show the IFS temperature perturbations $\Delta T$ due to gravity waves, calculated using the method described in Section 2.5.2. In the horizontal cross section (Fig. 3c), elongated, bow-shaped phase lines with moderate maximum values of $\Delta T = \pm 2$ K are situated along the STJ and are touched by the outermost part of the research flight ST10. In the vertical cross section (Fig. 3d), these phase lines reach from the upper edge of the poleward side of the tropopause fold diagonally into the lower stratosphere. At about 20 km, these phase lines interfere and combine with other phase lines with larger amplitudes in $\Delta T$. Most probably, these gravity waves are from other sources. Further phase lines with higher $\Delta T$ that originate near the ground

between 66°W and 74°W and extend further to stratospheric altitudes are the consequence of mountain waves above the southern Andes. At altitudes higher than 20 km, they interfere and combine with other phase lines to a complex entity. The sources of this gravity wave mix are probably the horizontal propagation of orographic waves, secondary waves, and/or non-orographic gravity waves near the PFJ, PNJ, and STJ.

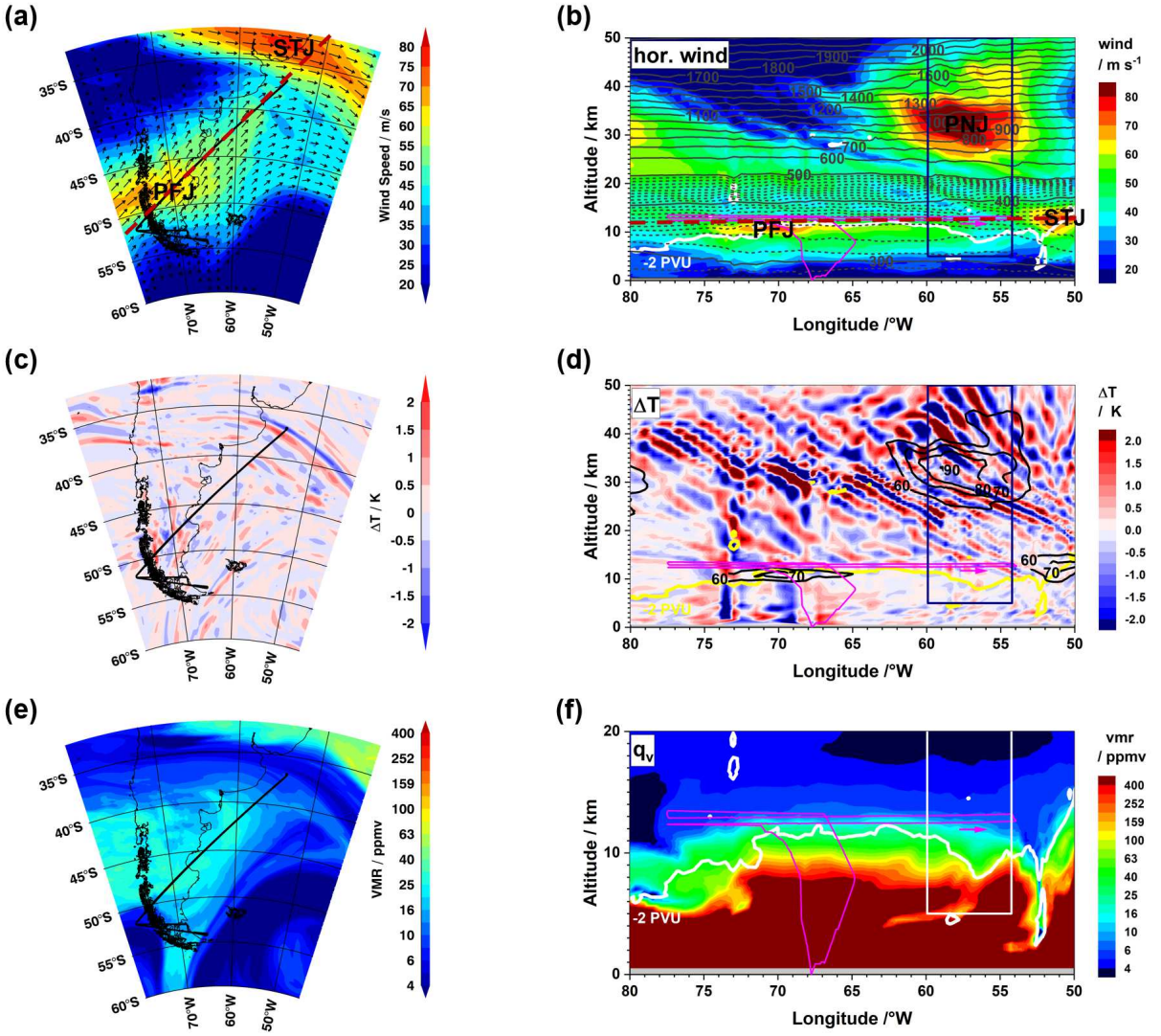


**Figure 3.** Horizontal (at 200 hPa or ~12 km altitude) and vertical cross sections of the ECMWF IFS data on 17 September 2019 02 UTC. Horizontal wind speed (a,b) and direction (arrows in a), temperature perturbation (ΔT between $T_{Co}1279$ and T106 resolution data) (c, d), and specific humidity (e, f). Isolines of potential temperature are superimposed in grey in panel (b) (solid grey lines: ΔΘ=100 K, dashed grey lines: ΔΘ=10 K). The -2 PVU isoline is indicated by white/yellow lines in the vertical cross sections. Selected isolines of horizontal wind (black solid lines, in m $s^{-1}$) are overlaid in panel (d). The flight track is indicated by black/magenta solid lines in the horizontal/vertical cross sections. Red dashed lines in panels (a, b) indicate the intersection between the horizontal and vertical cross sections shown in the left and right column, respectively.

Blue and white boxes in (b,d) and (f), respectively, highlight the "focus region" (see text). PFJ=polar front jet, STJ=subtropical jet, PNJ=polar night jet.

The distribution of specific humidity is shown in Figures 3e and 3f. In Figure 3e, higher water vapor mixing ratios in the lower stratosphere at ~12 km between about 38°S and 50°S above the Pacific, Andes and Patagonia are related to the ridge seen in Figure 2. Dry air masses in the south-east are due to the fact that the 200 hPa surface is here in the stratosphere above the low-pressure system. In the north-east, high specific humidity indicates the step in the tropopause at the STJ. An elongated dry band from ~35°S in the west to ~40°S in the east corresponds to the tropopause fold seen in Figure 2. In the vertical cross section in Figure 3f, the steep increase from low and approximately constant stratospheric water vapour mixing ratios towards tropospheric values begins mostly a few kilometres above the tropopause. Around the tropopause, variable water vapor mixing ratios of the order of 10 ppmv to 50 ppmv and strong vertical gradients of specific humidity are found (greenish colored region in Fig. 3f). In the vicinity of the tropopause fold between 51°W and 55°W, dry air masses reach down to altitudes lower than 3 km. In the intrusion, moist air masses remain high whilst the dynamical tropopause is lowered. A comparatively dry band stretches from the intrusion down to ~ 5 km altitude and then horizontally to the south-west.

In summary, the phase lines probed in the focus region of the flight ST10 reach from the upper edge of the poleward side of a tropopause fold into the lower stratosphere. They are situated in a region affected by horizontal wind shear between the PFJ and STJ and above an intrusion of stratospheric air into the tropopause.

### 4.2 Comparison of IFS with GLORIA and ALIMA

A remarkable agreement is found for the comparison of the temperature perturbations extracted from the GLORIA and ALIMA (Fig. 4a) data with ones from the IFS data (Fig. 4b). As discussed in Section 2.5.2, a different approach for extracting temperature perturbations $\Delta T$ by gravity waves is applied here to ensure a consistent de-trending of all data sets by using the same approach. Naturally, a one-to-one correspondence between the observations and the forecast/analysis data cannot be expected. Nevertheless, all major phase line patterns simulated by the IFS correspond to phase lines in the airborne remote-sensing observations in the troposphere as well as stratosphere: In particular, (i) the cold anomaly around flight altitude before the distance of 2800 km, (ii) the warm phase line stretching from an altitude of ~16 km altitude at 2500 km downwards to ~11 km altitude at 3200 km, (iii) and another large warm phase line at higher altitudes, reaching from ~30 km altitude at 2500 km downwards to ~24 km altitude at 3200 km. Further corresponding warm and cold anomalies $\Delta T$ are found in the model data and observations at all altitudes. The amplitudes of the temperature perturbations $\Delta T$ compare well between the IFS data and observations. Slightly lower maximum amplitudes in the IFS data, mainly below 25 km, can be explained by the limited model resolution. Note that the major phase lines in the IFS data are aligned in an almost identical orientation compared with the airborne observations.

Along the dynamical tropopause, a weak temperature minimum is found consistently in both the observations and model data and confirms the location of the thermal tropopause in the IFS data. Missing data points in the GLORIA data before ~2550 km and, below the tropopause beyond a distance of 2950 km, are due to a change in the GLORIA measurement mode and opaque tropospheric clouds, respectively. Note that the shape of the dynamical tropopause appears

different here when compared with Figure 3, since the IFS data are interpolated here at the measurement times and, below flight level, along the geolocations of the tangent points of the GLORIA observations (compare Fig. 1).

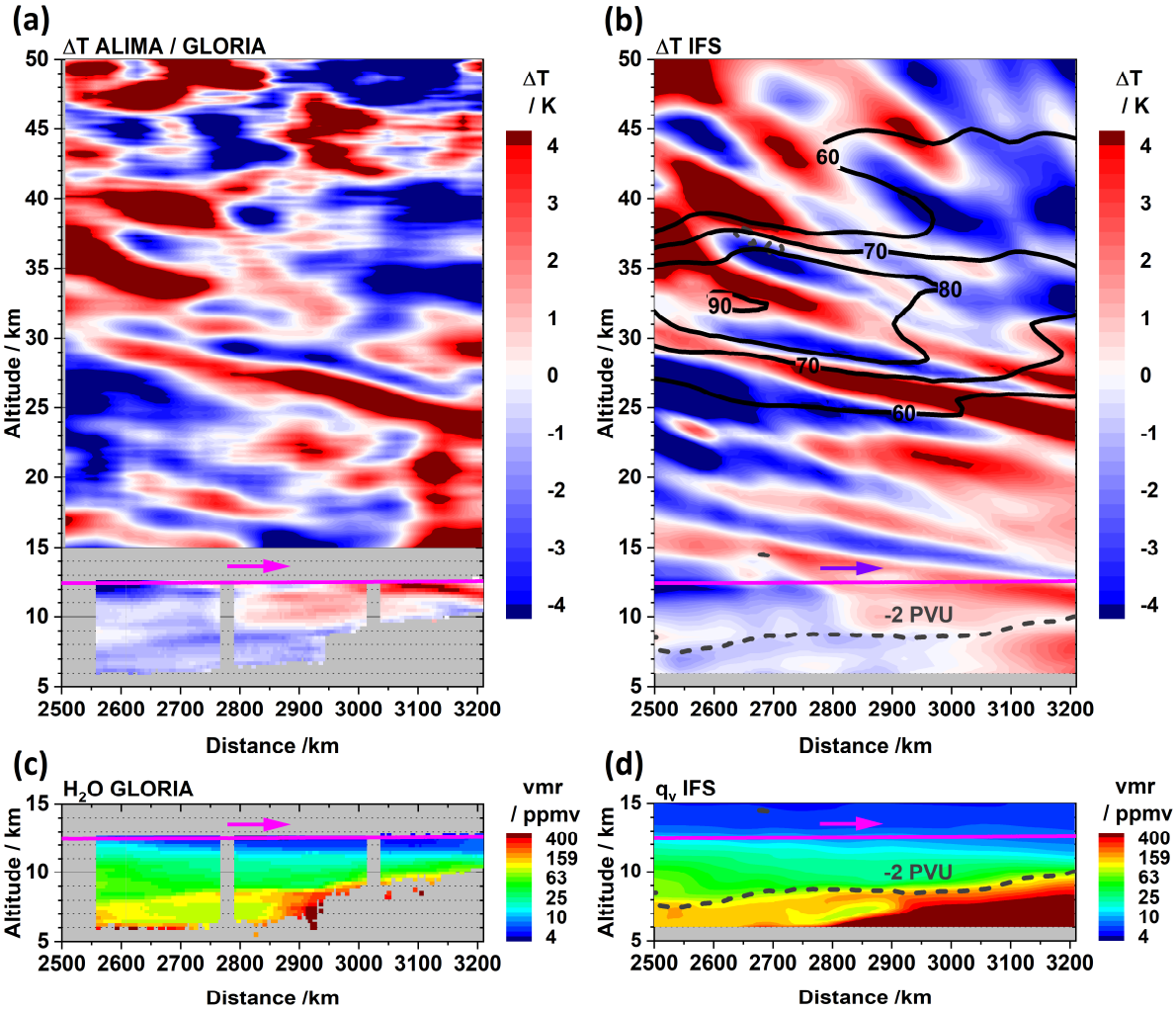


**Figure 4.** Observed and forecasted temperature perturbations. (a) Temperature perturbation calculated from ALIMA (above 15 km) and GLORIA (below 12.5 km). (b) Temperature perturbation calculated from IFS data. (c) GLORIA water vapor and (d) IFS specific humidity for the same flight section. For details of the comparison, see Section 2.5.1 and 2.5.2. HALO flight altitude (magenta solid line, all panels), selected isolines of horizontal wind (black solid lines in (b), in m $s^{-1}$), and dynamical tropopause (dashed gray solid lines in (b, d)).

A satisfying agreement is also found between the structures seen in GLORIA water vapor and IFS specific humidity (Fig. 4c, d). The transition from moist tropospheric to dry stratospheric water vapor mixing ratios in the intrusion seen in the observations is consistently reproduced by the model. A dry filamentary structure below the tropopause prior to a distance of 2900 km agrees

at least qualitatively in the two datasets. Consistent with other studies (e.g. Stenke et al., 2008; Dyroff et al., 2015; Woiwode et al., 2020; Bland et al., 2021) a systematic moist bias is found in the model data in the entire region. However, the comparison confirms that the tropopause, the structure of the intrusion, and the absolute mixing ratios are simulated by the IFS in a realistic way.

### 4.3 Evolution of non-orographic gravity waves

In Figure 5, various diagnostics display the temporal evolution of the simulated non-orographic gravity waves and the jet stream merging event during central part of the flight at 02 UTC on 17 September 2019 (1st row) and 5 h (2nd row), 10 h (3rd row) and 19 hours (4th row) before. In order to follow the actual temporal sequence of the event, one has to read Figure 5 from bottom to top.

At the time HALO flew through the flight segment we are focusing on (the central time of the flight), phase lines with moderate amplitudes $\Delta T$ extend from the upper edge of the poleward side of the tropopause fold into the lower stratosphere and cross the flight path as shown in Figure 5a. At this time, the merging of the jet streams is in full progress. In the western half of the plot the PFJ is almost perpendicular to the STJ and in the eastern half the PFJ has aligned approximately parallel to the STJ both at flight level and in the upper troposphere (compare Fig. 5a with Fig. 5c, d).

Phase lines with notably larger $\Delta T$ at the tropopause fold (Fig. 5e) and at flight level (Fig. 5f) are found five hours earlier. At this time, upward and pronounced downward pointing phase lines extend from the shear region in the tropopause fold into the lower stratosphere and the troposphere, respectively (Fig. 5e). In the lowermost stratosphere, these phase lines stretch horizontally across more than 3000 km in west-east direction along the STJ (Fig. 5f). In the eastern part of Figure 5f, southwest-northeast oriented phase lines are connected with this bow-shaped gravity wave pattern (Fig. 5g). They seem to be related to the cyclonically curved PFJ over the Atlantic Ocean. At this time, the main part of the PFJ is aligned approximately perpendicular to the STJ in the lowermost stratosphere (Fig. 5g) and troposphere (Fig. 5h), while a smaller pronounced jet streak at the eastern part of the PFJ aligns already with the STJ.

Ten hours before the central time of the flight (Fig. 5i) and west of ~55.3°W, a “fishbone” pattern of phase lines (compare Vadas et al., 2018) is seen in the vertical cross section. At this time, a sequence of 3 warm and 2 cold interleaved upward- and downward pointing phase fronts can be clearly identified and stretch from the shear region in the tropopause fold in south-westward direction into the lower stratosphere and the troposphere. The same sequence of phase fronts is identified in the horizontal cross section in the lowermost stratosphere (Fig. 5j). A weaker, but clearly discernible pattern is found in the vertical domain in opposite direction (Fig. 5i), thus forming an “X-shaped” structure centred at ~55.3°W and an altitude of ~8 km. Also here, corresponding phase lines are seen in the horizontal domain in Fig. 5j. At the same time, the PFJ is oriented in a south to south-west direction above Patagonia (Fig. 5k, l). The smaller streak at the eastern side of the PFJ produces a confined local horizontal wind maximum that encounters the STJ approximately perpendicularly.

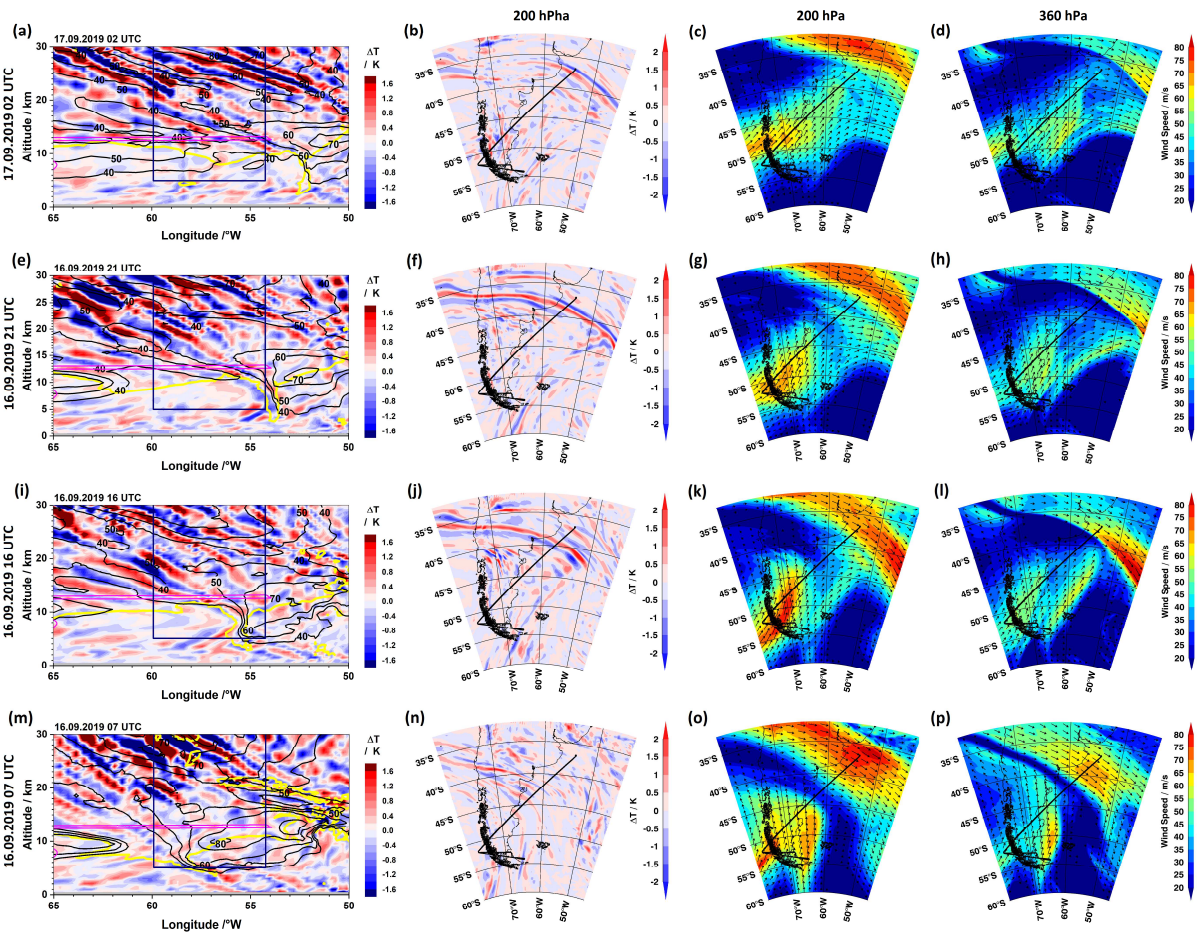


**Figure 5.** Evolution of non-orographic gravity waves and jet stream merging event in IFS data at central time of the flight (1st row) and 5 h (2nd row), 10 h (3rd row), and 19 h (4th row) before. (a, e, i, m) Vertical distributions of temperature perturbation along main axis of flight from 50°W to 65°W. (b, f, j, n) Temperature perturbation at 200 hPa (~ 12 km altitude). Horizontal wind speed and direction (c, g, k, o) at 200 hPa (~ 12 km altitude) and (d, h, l, p) at 360 hPa (~8 km). Selected isolines of horizontal wind (black solid lines, in m $s^{-1}$) and the -2 PVU isoline (yellow solid line) are overlaid in the vertical cross sections. The flight track is indicated by magenta/black solid lines in the vertical/horizontal cross sections.

Weak, but still discernible temperature perturbation ΔT in form of coherent phase lines are found nineteen hours before the central time of the flight (Fig. 5m, n). We show this particular time step to document the "initial" situation, since the bow-shaped phase lines become notably more pronounced in the subsequent time steps. Note the opposite orientation of the PFJ with respect to the STJ in the lowermost stratosphere and upper troposphere over northern Argentina and the Pacific Ocean (Fig. 5o, p). At 360 hPa, these jets are oriented fully antiparallel. In between, a narrow band of low wind speeds and strong horizontal wind shear is forecasted by the IFS. The jet streak in the east as seen in the previous panels is more developed here and joins from the south with the PFJ.

A full change of the PFJ direction from predominantly antiparallel to parallel with respect to the STJ and the temporal evolution of a strongly sheared tropopause fold are documented in Figure 5 when read from bottom to top. Gravity waves are excited along the strongly diverging flow where the PFJ impinges and merges with the STJ. As a result, gravity wave-induced temperature perturbations ΔT appear along the sheared tropopause fold over more than 3000 km in horizontal direction. The vertical sections in Figure 5 reveal that these waves are able to propagate from the tropopause level both upward into the stratosphere and downward into the troposphere.

A developed X-shaped pattern with moderate amplitudes in ΔT is found 10 hours before the central time of the flight (Fig. 5i). To analyze the specific body forces that accompany the excitation of these gravity waves, we investigate the acceleration and deceleration of the horizontal wind components u and v at this time in Figure 6. A strong deceleration ($\geq -6 \cdot 10^{-3}$ m s$^{-2}$) of the zonal wind and a strong acceleration ($< 6 \cdot 10^{-3}$ m s$^{-2}$) of the meridional wind are found in a small region within the tropopause fold as shown in Figures 6a, c. This is exactly at the location where the PFJ impinges the STJ (compare Fig. 5l) and where the X-shaped pattern is centered. In the horizontal domain (Fig. 6b,d), it is seen that the zonal deceleration and meridional acceleration occurs along the sheared bow-shaped band along the STJ as the PFJ impinges the STJ and reverses its direction (compare Fig. 5l). The deceleration and acceleration, respectively, are highest in the area where the jet streak along the PFJ "pushes" against the STJ.

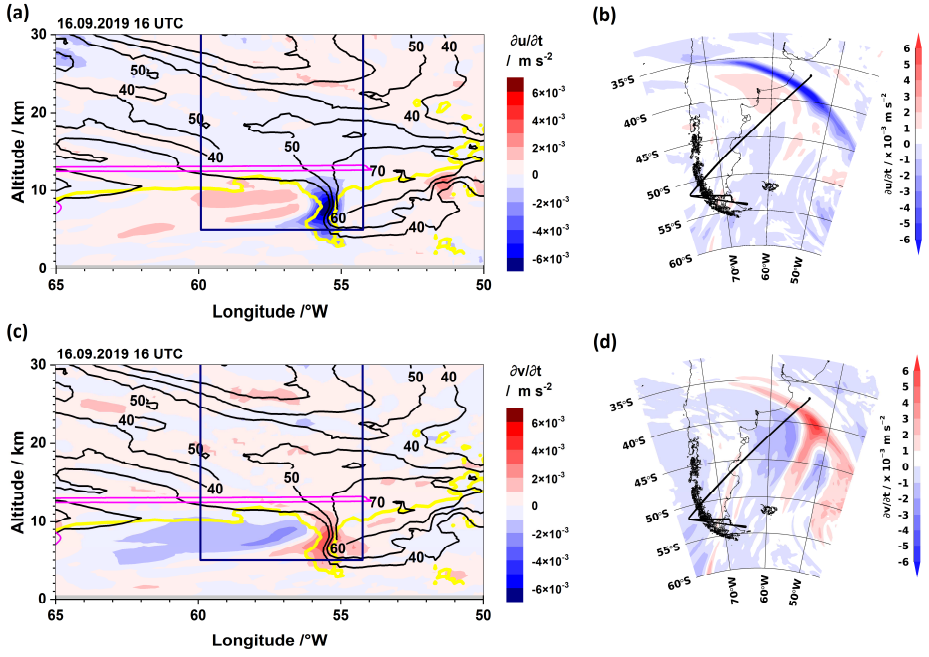


**Figure 6.** Tendencies in the horizontal wind components ten hours before the central time of the flight. The vertical and horizontal (at 360 hPa or ~8 km altitude) cross sections show the de-/acceleration of the (a,b) zonal and (c,d) meridional wind components. Selected isolines of horizontal wind speed (black solid lines, im m s$^{-1}$) and the -2 PVU isoline (yellow solid lines) are overlaid in panels a and c. The flight track is indicated by magenta/black solid lines in the vertical/horizontal cross sections.

Figure 7a shows a zoom into the X-shaped pattern of the phase lines. Isentropic backward trajectories are calculated with HYSPLIT to derive the paths of the different air masses colliding with each other in the tropopause fold 10 hours before the central time of the flight. In Figure 7b, the starting points of one trajectory at the poleward (blue) and one trajectory at the equatorward (red) side of the tropopause fold are marked. The starting points are located at 56°W and 55°W at an altitude of 8 km in the central region of the X-shaped pattern of the phase lines shown in Figure 7a. In Figure 7c, the backward trajectory starting at the equatorward side of the tropopause fold follows the STJ, while the trajectory starting from the poleward side follows the PFJ as it approaches the STJ. Figure 7d highlights the position of the backward trajectories in the horizontal wind field nine hours before the starting point (compare Fig. 5, 4th row). Here, the location of the backward trajectory from the poleward side coincides with the edge of the maximum in wind speed of the jet streak along the PFJ as it approaches the STJ.

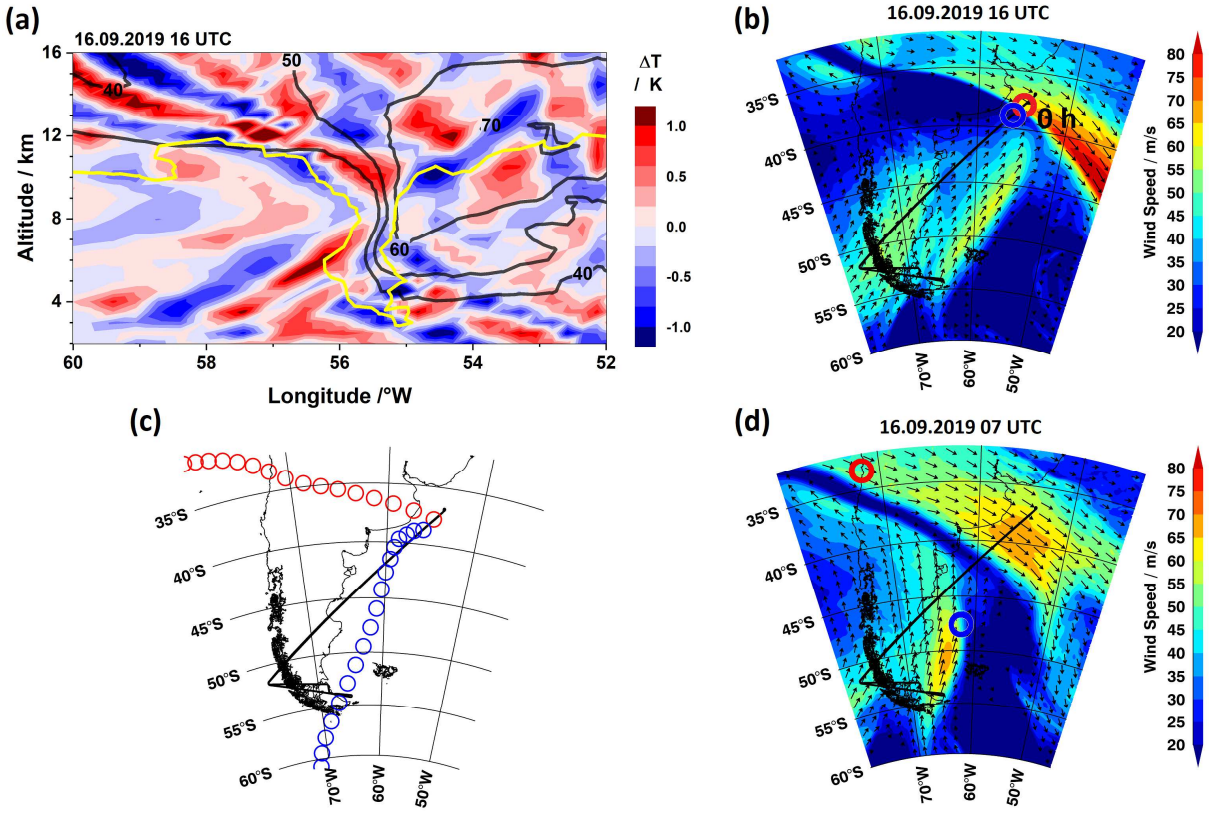


**Figure 7.** Zoom into "X-shaped" phase line pattern ten hours before the central time of the flight and HYSPLIT isentropic backward trajectories starting in the center region of the structure. (a) Vertical distribution of temperature perturbation along main axis of flight from 60°W to 52°W together with isolines of horizontal wind (black solid lines, in m $s^{-1}$) and -2 PVU isoline (yellow solid line). (b) Horizontal wind speed and direction at 360 hPa (~ 8 km altitude) at starting time of trajectories. (c) Geolocations of trajectories (spacing between circles: 1 h, time range: ≥ 17 h). (d) Horizontal wind speed and direction at 360 hPa (~ 8 km altitude) at 9 hours before trajectory starting point. The flight track is indicated by magenta/black solid lines in the vertical/horizontal cross sections.

### 4.4 Embedded small-scale gravity waves and turbulence

The BAHAMAS in situ observations provide a highly resolved view at the temperature and the wind components at flight level and down to scales relevant for turbulence (Fig. 8). In the considered flight section, the temperature increases by about 10 K toward the northeast before it falls slightly in the vicinity of the northernmost waypoint (Fig. 8a). GLORIA (magenta circles) and BAHAMAS (black line) temperatures are in excellent agreement beyond a distance of 2800 km. Prior to 2800 km, slight differences between BAHAMAS and GLORIA can be explained by local temperature variations which are seen differently by the two measurement techniques (i.e. BAHAMAS exactly at flight track and GLORIA in limb geometry to the right hand side). A horizontal wavelength along the flight direction of ~300 km is estimated for the non-orographic gravity wave from the observations. Due to the higher temporal and spatial resolution, BAHAMAS resolves much more small-scale fluctuations in the temperature distribution than the GLORIA remote sensing observations. The overall variation of the zonal and meridional wind components and lots of fine structures are seen in the BAHAMAS data in Fig 8c, e. In the vertical wind, the BAHAMAS data show considerable high-frequency variations down to the sub-kilometer scale and peak values exceeding ± 4 m/s in a short 25 km long interval starting at a distance of 3000 km (Fig. 8g).

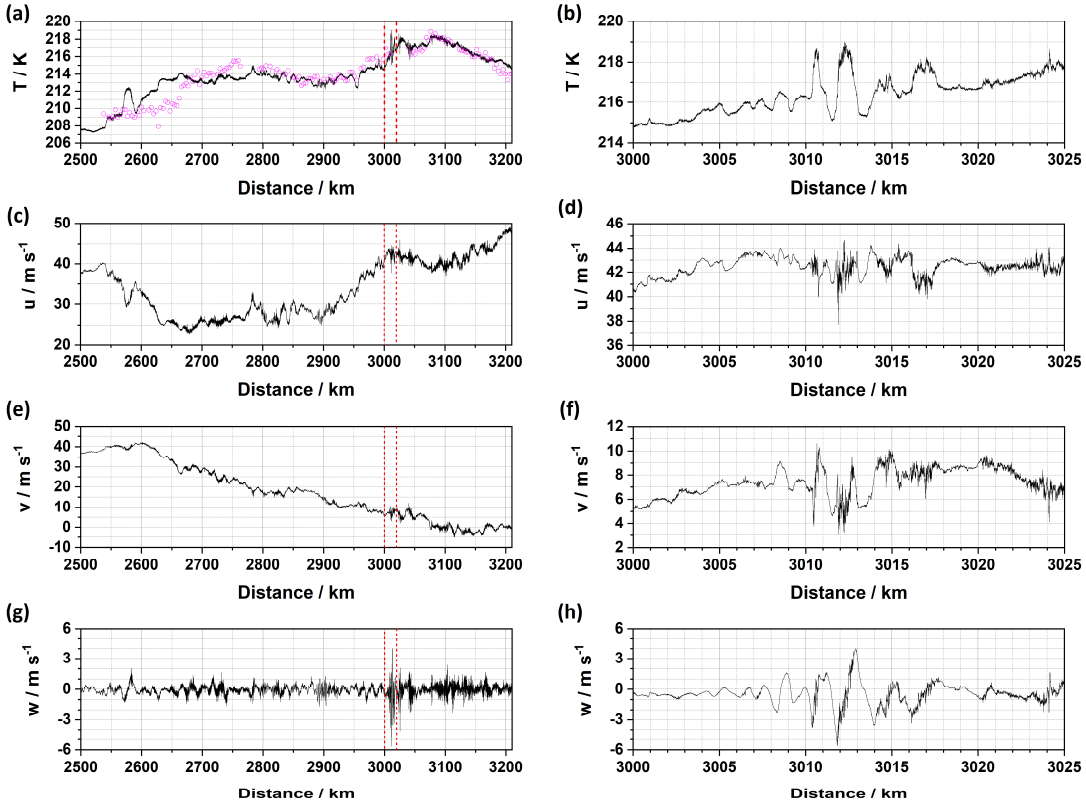


**Figure 8.** BAHAMAS in situ observations of meteorological variables during flight section in focus (left column) and zoom at location of Kelvin-Helmholtz wave (right column). Black solid lines indicate (a, b) temperature, (c, d) zonal wind, (e, f) meridional wind, and (g, h) vertical wind. GLORIA observations are shown in panel (a) in magenta. Red dashed lines in the left columns mark the section shown in the right column.

A zoom into this region with the strongest variations in vertical wind is shown in the right column of Figure 8. An oscillation is seen in the temperature data with a horizontal wavelength of ~ 2 km and a maximum peak-to-peak amplitude of 4 K (Fig. 8b). Further fine structures well below horizontal scales of 100 m are superimposed. Note, due to the high-resolution 100 Hz data, the spatial resolution of the BAHAMAS observations is about 2.5 m in the horizontal. Complex structures with a similar periodicity and further fine structures are found also in the horizontal wind components (Fig. 8d, f). A developed oscillation in the vertical wind component (Fig. 8h) with a horizontal wavelength of ~2 km and a phase shift of $\pi/2$ with respect to the oscillation seen in the temperature data (Fig. 8b) indicates that a Kelvin-Helmholtz wave at the lower end of the gravity wave spectrum is seen here. Notable variations on turbulent scales are superimposed on the Kelvin-Helmholtz wave and in its vicinity and indicate that turbulent processes are in progress here.

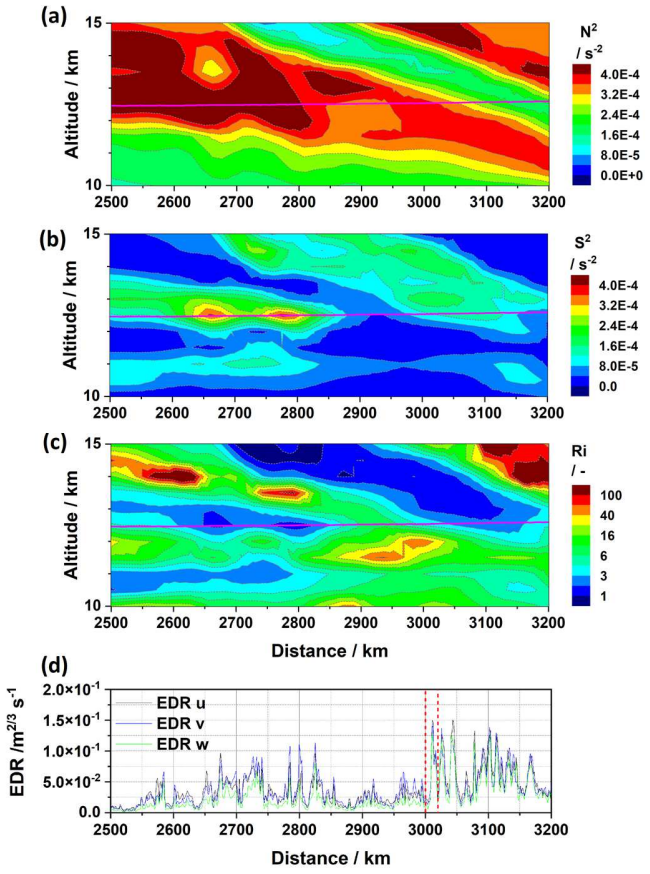


**Figure 9.** Comparison of (a) squared Brunt–Väisälä frequency ($N^2$), (b) squared shear parameter ($S^2$) and (c) gradient Richardson number (Ri) calculated from the IFS data around flight level. (d) EDR calculated from the 100 Hz BAHAMAS data for the three wind components. Note, "u" and "v" refer to the forward and sideward direction with respect to the flight path in this context. The flight altitude is indicated by magenta solid lines in (a, b, c).

To investigate the situation of the Kelvin-Helmholtz wave and turbulence, the squared Brunt–Väisälä frequency ($N^2$), the squared shear parameter ($S^2$) and the gradient Richardson

number (Ri) calculated from the IFS data are shown around flight altitude in Figure 9. These quantities are shown together with the cube root of the energy dissipation rates (EDR) calculated from the BAHAMAS data, see Dörnbrack et al. (2022). The $N^2$ distribution (Fig. 9a) shows tilted bands of enhanced and decreased static stability due to the modulation by the non-orographic gravity waves (compare Fig. 4a, b). A similarly tilted pattern is also found in the distribution of $S^2$ (Fig. 9b). The combination of the modulated static stability and the regions of locally enhanced wind shear results in patches of $R_i$ values lower than ~3 (Fig. 9c). Typically, $R_i$ values less than 0.25 indicate turbulence generation. However, Ri values calculated from model data rarely show such low values due to limited model resolution and interpolation losses. Hence, the minimum of the $R_i$ values are compared qualitatively with EDR. These patches intersect with the flight altitude between 2550 km and 2850 km, and between 2950 km and 3200 km, and coincide well with episodes where EDR values calculated from the BAHAMAS data for the three wind components approach and exceed 0.05 $m^{2/3}$ $s^{-1}$ and locally reach maximum values of 0.10 $m^{2/3}$ $s^{-1}$ to 0.15 $m^{2/3}$ $s^{-1}$ (Fig. 9d). According to Bramberger et al. (2018, 2020), such values are indicative of light to moderate CAT for a HALO-size aircraft. In summary, the combination of the static stability, modulated by the non-orographic gravity, and locally enchaned shear formed localized regions with small values of $R_i$, where flow instabilities can grow rapidly. Overall, this burst of turbulence was not a truly severe event, most likely due to the long horizontal wavelength that causes the change in stratospheric airflow.

Overall, the BAHAMAS data show good agreement with GLORIA on mesoscale, but resolve much more fine structures for a greater variety of parameters that are relevant for gravity waves. Observations of light to moderate CAT and a Kelvin Helmholtz wave at flight altitude confirm the crucial role of non-orographic gravity waves in modulating the ambient airflow and supporting Kelving Helmholtz waves, turbulence, and thus a cascading of kinetic energy from larger to smaller scales.

### 4.5 Wave analysis

In order to quantify the wave properties at flight level, two about 1000 km long sections are analyzed. These sections are outermost parts of the long outbound leg 2 and inbound leg 3 of ST10 according to Table S1 of Dörnbrack et al. (2022). Their southernmost way points are at -44.0°S, -63.2°W and -44.6°S, -63.9°W, respectively (compare Fig. 3, right column). Thus, these sections reach ~300 km further to the south-west than the sections shown in Figures 4 and 8, but are otherwise practically identical. The outbound leg 2 was flown at about 12.5 km altitude, the inbound leg 3 at 13.0 km altitude, respectively (see Fig. 3).

The wave energy fluxes are determined by means of methods as documented in Smith et al. (2008, 2016) and applied to the SouthTRAC data in Dörnbrack et al. (2022). For this purpose, the 1000 km legs are divided into three equal sections, each about 340 km in length. Table 1 lists the horizontal and vertical wave energy fluxes for the both northernmost sections (i.e. the second half of panels shown in the left column of Fig. 8) . The vertical energy fluxes $EF_z$ are positive, the zonal and meridional wave energy fluxes $EF_x$ and $EF_y$ are negative. First of all, these numbers indicate gravity waves propagating vertically upward and travelling against the mean flow. Second, all wave energy fluxes have small values compared to those achieved over mountains that normally exceed 2 W $m^{-2}$ for $EF_z$ and -100 W $m^{-2}$ for $EF_x$ or $EF_y$ (Kruse and Smith 2015, Dörnbrack et al. 2022). Consistent with the upward propagation of wave energy are the negative vertical fluxes of horizontal momentum $MF_x$ and $MF_y$.

636 **Table 1.** Zonal, meridional, and vertical wave energy fluxes $EF_x$, $EF_y$, and $EF_z$ along the
637 northernmost sections of leg 2 and 3 (each 340 km in length) of ST10 calculated from 10 Hz
638 BAHAMAS data. Further quantities computed along these sections are the zonal and meridional
639 momentum fluxes $MF_x$ and $MF_y$ as well as the scalar product of the horizontal wind vector **U** with
640 the horizontal momentum flux **MF** (from Dörnbrack et al., 2022).

| | $EF_x$ / W m$^{-2}$ | $EF_y$ / W m$^{-2}$ | $EF_z$ / W m$^{-2}$ | -**U**·**MF** / W m$^{-2}$ | $MF_x$ / mPa | $MF_y$ / mPa |
|---|---|---|---|---|---|---|
| Leg 2 | -10.6 | -4.8 | 0.30 | 1.63 | -41.4 | -8.5 |
| Leg 3 | -6.0 | -7.4 | 0.16 | 0.38 | -2.9 | -24.0 |

641 The wave energy fluxes are relatively small, the magnitude of the $MF_x$ values found here
642 is of the same order of magnitude as the majority of $MF_x$ values observed during the DEEPWAVE
643 campaign above New Zealand (compare Fig. 5b in Smith et al., 2016). Furthermore, the reader is
644 reminded of the large scale of the event analyzed here. While the $EF_x$ or $EF_y$ are by more than one
645 order of magnitude smaller when compared with typical mountain waves, the area covered by the
646 event analyzed here is much larger when compared to typical mountain waves. Provided that the
647 energy fluxes found here are representative for the whole area covered by the phase fronts (see
648 Fig. 5, 2$^{nd}$ column), we speculate that the associated total energy that is transported per unit time
649 (i.e. the product of energy flux and covered area, in W) is comparable to a more localized mountain
650 wave event.

651 For a linear, stationary non-dissipative wave the Eliassen-Palm relation predicts that the
652 vertical wave energy flux $EF_z$ equals the negative scalar product of the horizontal wind vector **U**
653 with the momentum flux **MF** (Eliassen and Palm, 1961). This quantity, as listed in the fifth column
654 of Table 1, is always a factor 2 to 5 larger than $EF_z$ suggesting the observed gravity waves cannot
655 be steady or non-dissipative. This is not a surprising result, but a confirming one, since the source
656 of the waves are the forces associated with the deceleration of the PFJ as it impinges on the STJ.

657 **Table 2**. Energy densities $KE_x$, $KE_y$, $KE_{HP}$, $KE_z$, PE in J m$^{-3}$ as well as the dimensionless ratios
658 $KHR = KE_{HP}/KE_H$, $KER = KE_z/KE_{HP}$, and $EQR = PE/(KE_z + KE_{HP})$ calculated from 10 Hz
659 BAHAMAS data.

| | $KE_x$ | $KE_y$ | $KE_{HP}$ | $KE_z$ | PE | KHR | KER | EQR |
|---|---|---|---|---|---|---|---|---|
| Leg 2 | 0.81 | 0.49 | 0.08 | 0.03 | 0.83 | 0.06 | 0.36 | 7.59 |
| Leg 3 | 0.49 | 2.05 | 0.05 | 0.02 | 0.44 | 0.02 | 0.39 | 5.67 |

660 In addition, energy densities are computed along the two northernmost sections of legs 2
661 and 3 of each 340 km length (Table 2). The energies densities are quadratic quantities (Gill 1982)
662 and are computed as suggested by Smith et al. (2008, Eqs. 13 -18) but here divided by the length
663 of the respective sections, i.e. they are given in J m$^{-3}$. The $KE_x$ and $KE_y$ components of the
664 horizontal energy $KE_H = KE_x + KE_y$ are significantly larger compared to the wave-induced
665 horizontal kinetic energy density $KE_{HP}$ leading to ratio $KHR << 1$. The dominance of $KE_H$ is due
666 to large-scale variations of the dynamical variables due to atmospheric processes. Interestingly,

667 $KE_{HP}$ and $KE_Z$ have the same order of magnitude, but $KE_{HP}$ is always larger than $KE_Z$, leading to
668 a ratio KER < 1. These results indicate that horizontal air parcel orbits dominate the measured
669 gravity waves, suggesting upward propagating inertial gravity waves as the ones that are detected
670 at flight level.

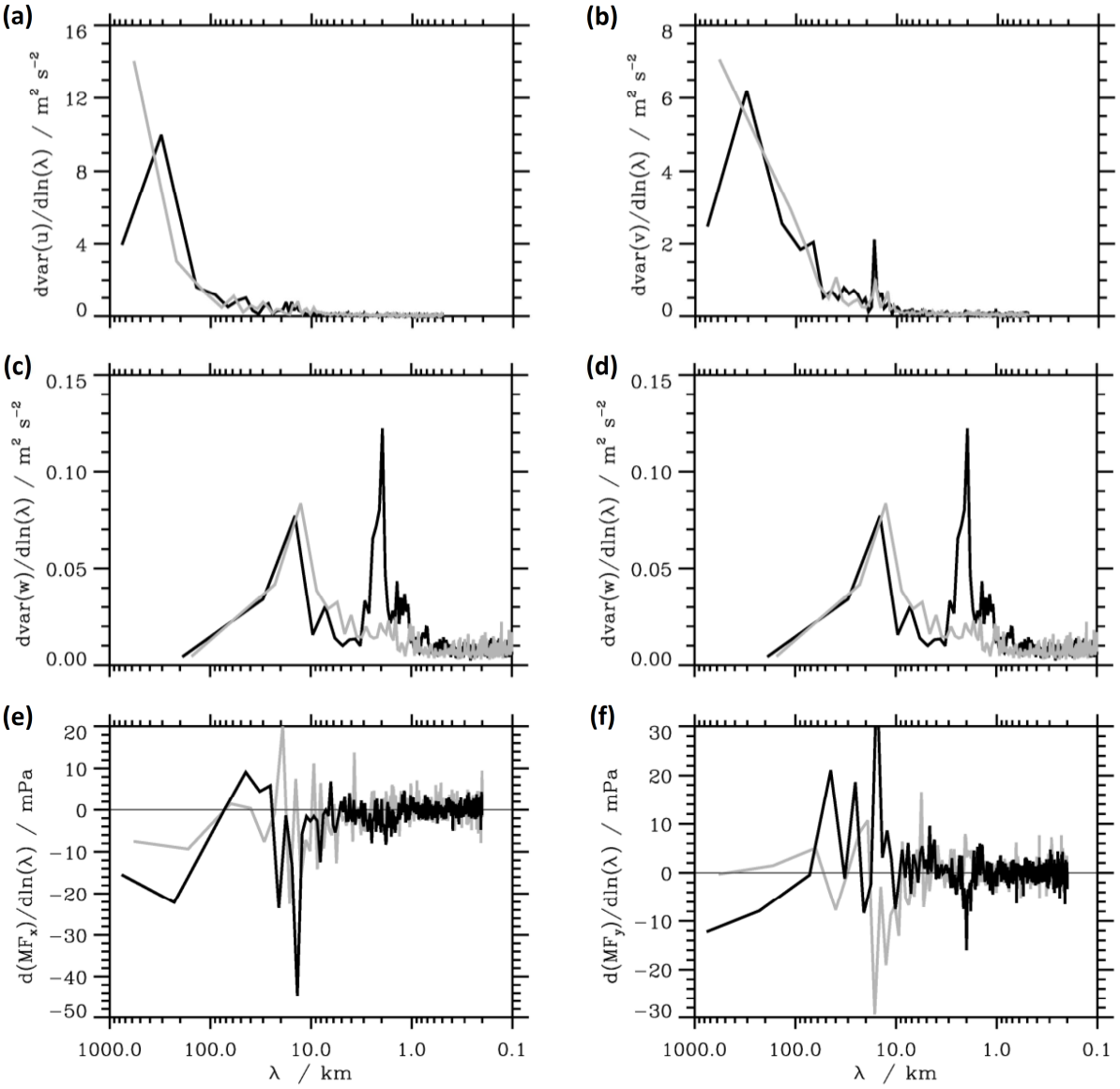


671

672 **Figure 10.** Binned power spectra of the zonal and meridional wind components (upper row), the
673 vertical wind component (middle row, both panels are equal), and the zonal and meridional
674 momentum fluxes (bottom row) as derived from the BAHAMAS data. The black curves are for
675 the outbound leg 2, the gray curves for the inbound leg 3 flown along the same flight track as leg
676 2. Both analyzed legs are about 1000 km long.

677 In linear steady waves, the wave-induced kinetic energy density KE = ($KE_z$ + $KE_{HP}$) should
678 balance the potential energy density PE resulting in an equipartition ratio EQR = 1. Here, EQR is

considerably larger than 1. This result is in very good agreement with the values as shown in Figure 14 of Smith et al. (2008). There, the large EQR values could be explained by partial wave reflection in the lower stratospheric levels. It is probably the shorter waves that are reflected in these layers as shown by the spectral analysis presented next.

Figure 10 shows the binned power spectra of the horizontal and vertical wind components u and v as well as those of the zonal and meridional momentum fluxes $MF_x$ and $MF_y$ for the two outermost sections of the legs 2 and 3 that are about 1000 km in length. It is known from other aircraft measurements (Kruse and Smith, 2015) that the spectra of the horizontal wind components are dominated by gravity waves longer than about 100 km. The same is true for our measurements. Only in the v spectra there is a peak with lower amplitude around 20 km. The power of the w spectrum is mainly in the wavelength range between 10 and 50 km. The remarkable result here is the lone peak in vertical power at 2 km horizontal wavelength, which is related to the instability that led to the CAT event associated with the Kelvin-Helmholtz wave. This peak is present in leg 2 of ST10, but it is absent when HALO passes this region again about 45 minutes later along leg 3, indicating the intermittent, erratic nature of the turbulence encountered. The absence of the peak at 2 km could also be due to the slightly higher flight level, suggesting that the turbulence event is vertically confined, a typical property of sporadically occurring Kelvin-Helmholtz billows. For both analyzed legs, horizontal momentum is mainly transported vertically by gravity waves longer than 100 km and by waves at horizontal wavelengths between 10 and 30 km in zonal direction and 10 and 70 km in meridional direction.

The spectra as displayed in Figure 10 suggest a vertical downward transport of horizontal momentum by the longer gravity waves (negative $MF_x$ and $MF_y$ for wavelengths longer than 100 km). Shorter waves along both legs contribute to the vertical momentum transport with variable signs and support the idea of partial wave reflection as mentioned above. The vertical wind spectra clearly indicate the existence of the short-wave instability at 2 km and suggest enhanced but small w-variances due to the turbulence encounter at scales smaller than 1 km.

## 5 Discussion and Conclusions

Airborne observations by the combination of the remote sensors GLORIA and ALIMA with the in situ sensor BAHAMAS at 100 Hz allowed us to resolve mesoscale fine structures of non-orographic gravity waves, Kelvin-Helmholtz waves and turbulence during a merger of the PFJ with the STJ. The timing, location and alignment of phase lines by the observed non-orographic gravity waves are reproduced well by 1-hourly deterministic short-term forecasts by the IFS at ~9 km horizontal resolution. In the temporal evolution in the IFS data, elongated phase fronts stretching along more than 3000 km in horizontal direction and emerging from a highly sheared region in a tropopause fold are identified as the PFJ impinges the STJ. Ten hours before the time of the observations, the IFS data show an X-shaped pattern of phase lines that point upward into the stratosphere and downward into the troposphere. To our best knowledge, such a phase line pattern in connection with a tropospheric jet stream merging event has not been documented before.

According to Vadas & Fritts (2001), spatially confined body forces in the atmosphere result in mean responses and, if the forcing is fast enough, in the creation of gravity waves. Vadas & Becker (2018) and Vadas et al., (2018) discuss characteristic “fishbone” patterns in temperature perturbations due to secondary gravity waves that propgagate upward and downward, and forward and backward away from the force. These gravity waves are excited by local body forces generated

by a primary gravity wave. Thereby, the acting force is a horizontal acceleration of the background flow, generated by the dissipation from the primary wave. In our case, the analysis of tendencies in the horizontal wind components shows strong deceleration in the zonal direction and acceleration in meridional direction as the PFJ impinges the STJ. Similar to the conditions discussed in the studies mentioned above, the consequence is a local body force acting exactly at the source region of the non-orographic gravity waves, i.e. the center of the X-shaped structure.

Moist processes are known to play an important role for gravity waves in baroclinic jet-front systems, resulting in a faster growth, earlier emerging, and larger amplitudes gravity waves which are fully coupled with dry modes (Wei and Zhang, 2014). Moist processes possibly play a role in the study presented here, but are not accessible to the observations and analysis here. Note however that GLORIA observed clouds in the vicinity of the tropopause fold (see high cut-off altitude in the GLORIA data in the troposphere due to clouds after 2950 km in Figure 3), thus supporting that moist processes might play a role here.

The analysis of zonal, meridional, and vertical wave energy and momentum fluxes based on the BAHAMAS data confirm that the probed portion of the non-orographic gravity waves propagates vertically upward and travels against the mean flow. The associated local wave energy fluxes and momentum fluxes are small when compared to those of typical, locally more confined mountain waves. However, provided that the conditions found in the section probed by the observations are representative for the large area covered by the phase fronts seen in the IFS data, such events might contribute significantly to energy redistribution in the upper troposphere and lower stratosphere. The spectra of the horizontal wind components are dominated by wavelengths larger than 100 km, while the power of the w spectrum is mainly in the wavelength range between 10 and 50 km (for details of the analysis of the BAHAMAS data, see Dörnbrack et al., 2022). A developed lone peak is clearly and consistently identified in vertical power at 2 km horizontal wavelength and corresponds with the instability that led to the CAT event associated with the Kelvin Helmholtz wave.

As shown by the IFS data, the modulation of static stability by the non-orographic gravity waves and tilted bands of locally enhanced shear between the merging jet streams result in patches of low gradient Richardson numbers that are supportive for CAT. Consistenly, episodes of light-to-moderate CAT (compare Bramberger et al., 2018, 2020) and Kelvin Helmholtz waves are observed at flight altitude in the 100 Hz BAHAMAS data in these regions. This suggests that the potential for such turbulence events is well accessible to established turbulence forecasting (e.g. Sharman et al., 2012, and references therein).

## Acknowledgments

The authors gratefully acknowledge the Federal Ministry of Education and Research of Germany (BMBF), which supported this study within the research initiative ROMIC II (project WASCLIM, grants 01LG1907A, 01LG1907D and 01LG1907E). We would like to thank the German Research Foundation (Deutsche Forschungsgemeinschaft, DFG project number 316646266) for funding parts of the SouthTRAC mission costs within the HALO SPP 1294. The authors especially acknowledge the SouthTRAC coordination and flight-planning teams, the GLORIA team from KIT and FZJ, the ALIMA team from DLR-IPA, and the DLR-FX team for planning and carrying out the flights and providing the observations. We thank the ECMWF for providing the meteorological data. Access to the operational ECMWF data was granted through the special project “Gravity Waves and Turbulence over the Andes” by AD. The authors thank the

NOAA Air Resources Laboratory (ARL) for the provision of the HYSPLIT transport and dispersion model and READY website (https://www.ready.noaa.gov) used in this publication.

The authors declare no conflicts of interests.

## Open Research

The generation of non-orographic gravity waves and turbulence by jet streams is complex and subject of ongoing research. Case studies that resolve mesocale fine-structures and turbulent scales help to understand the underlying processes and test state-of-the are weather forecasting systems.

## Data availability

The GLORIA, ALIMA and BAHAMAS observations and the ECMWF IFS data are available at DOI: 10.5445/IR/1000151856. For the ECMWF data, the terms of use by the ECMWF apply. The ECMWF data are furthermore available at https://www.ecmwf.int/en/forecasts. HYSPLIT trajectories are available via the READY website by the NOAA.

## References

Bland, J., Gray, S., Methven, J., & Forbes, R. (2021), Characterising extratropical near-tropopause analysis humidity biases and their radiative effects on temperature forecasts. *Q J R Meteorol Soc, 147*(741), 3878– 3898. doi.org/10.1002/qj.4150

Bramberger, M., Dörnbrack, A., Wilms, H., Gemsa, S., Raynor, K., & Sharman, R. (2018), Vertically Propagating Mountain Waves—A Hazard for High-Flying Aircraft? *Journal of Applied Meteorology and Climatology*, *57*(9), 1957-1975. doi.org/10.1175/JAMC-D-17-0340.1

Bramberger, M., Dörnbrack, A., Wilms, H., Ewald, F., & Sharman, R. (2020), Mountain-Wave Turbulence Encounter of the Research Aircraft HALO above Iceland. *Journal of Applied Meteorology and Climatology*, *59*(3), 567-588. doi.org/10.1175/JAMC-D-19-0079.1

Dörnbrack, A., Gisinger, S., Kaifler, N., Portele, T. C., Bramberger, M., Rapp, M., Gerding, M., Söder, J., Žagar, N., & Jelić, N. (2018), Gravity Waves excited during a Minor Sudden Stratospheric Warming. *Atmos. Chem. Phys., 18*, 12915-12931. doi.org/10.5194/acp-18-12915-2018

Dörnbrack, A., Kaifler, B., Kaifler, N., Rapp, M., Wildmann, N., Garhammer, M., Ohlman, K., Payne, J., Sandercock, M., & E. Austin (2020), Unusual appearance of mother-of-pearl clouds above El Calafate, Argentina (50° 21′ S, 72° 16′ W). *Weather, 75*, 378-388. doi.org/10.1002/wea.3863

Dörnbrack, A. (2021), Stratospheric mountain waves trailing across Northern Europe. *Journal of the Atmospheric Sciences*, *78*, 2835-2857. doi.org/10.1175/JAS-D-20-0312.1

Dörnbrack, A., Bechtold, P., & Schumann, U. (2022). High-resolution aircraft observations of turbulence and waves in the free atmosphere and comparison with global model predictions. *Journal of Geophysical Research: Atmospheres*, 127, e2022JD036654. https://doi.org/10.1029/2022JD036654

Dörnbrack, A., Eckermann, S. D., Williams, B. P., & Haggerty, J. (2022), Stratospheric gravity waves excited by propagating Rossby wave trains – A DEEPWAVE case study. *Journal of the Atmospheric Sciences*, *79*, 567-591. doi.org/10.1175/JAS-D-21-0057.1

Draxler, R. R., & Hess, G. D. (1998), An overview of the HYSPLIT_4 modeling system of trajectories, dispersion, and deposition. *Aust. Meteor. Mag., 47*, 295–308

Dyroff, C., Zahn, A., Christner, E., Forbes, R., Tompkins, A. M., & van Velthoven, P. F. J. (2015), Comparison of ECMWF analysis and forecast humidity data with CARIBIC upper troposphere and lower stratosphere observations. *Q. J. Roy. Meteor. Soc., 141*, 833–844. doi.org/10.1002/qj.2400

Ehard, B., Kaifler, B., Kaifler, N., & Rapp, M. (2015), Evaluation of methods for gravity wave extraction from middle-atmospheric lidar temperature measurements. *Atmos. Meas. Tech., 8*, 4645–4655. doi.org/10.5194/amt-8-4645-2015

Eliassen, A., & Palm, E. (1961). On the transfer of energy in stationary mountain waves. *Geofys. Publ.*, 22(3), 1-23

Friedl-Vallon, F., Gulde, T., Hase, F., Kleinert, A., Kulessa, T., Maucher, G., Neubert, T., Olschewski, F., Piesch, C., Preusse, P., Rongen, H., Sartorius, C., Schneider, H., Schönfeld, A., Tan, V., Bayer, N., Blank, J., Dapp, R., Ebersoldt, A., Fischer, H., Graf, F., Guggenmoser, T., Höpfner, M., Kaufmann, M., Kretschmer, E., Latzko, T., Nordmeyer, H., Oelhaf, H., Orphal, J., Riese, M., Schardt, G., Schillings, J., Sha, M. K., Suminska-Ebersoldt, O., & Ungermann, J. (2014), Instrument concept of the imaging Fourier transform spectrometer GLORIA. *Atmos. Meas. Tech., 7*, 3565–3577. doi.org/10.5194/amt-7-3565-2014

Gettelman, A., Hoor, P., Pan, L. L., Randel, W. J., Hegglin, M. I., & Birner, T. (2011), The extratropical upper troposphere and lower stratosphere. *Rev. Geophys., 49*, RG3003. doi.org/10.1029/2011RG000355

Giez, A., Mallaun, C., Zöger, M., Dörnbrack, A., & Schumann, U. (2017), Static pressure from aircraft trailing-cone measurements and numerical weatherprediction analysis. *J. Aircr., 54*, 1728–1737, doi.org/10.2514/1.C034084

Giez, A., Zöger, M., Dreiling, V., & Mallaun, C. (2019), Static source error calibration of a nose boom mounted air data system on an atmospheric research aircraft using the trailing cone method. *DLR Internal Rep. 2019-07*, 87 pp.

Giez, A., Mallaun, C., Nenakhov, V., & Zöger, M. (2021), Calibration of a Nose Boom Mounted Airflow Sensor on an Atmospheric Research Aircraft by Inflight Maneuvers (Tech. Rep. No. 2021-17). *Oberpfaffenhofen: DLR.* Retrieved from https://elib.dlr.de/145969/

Gill, A. E. (1982), Atmosphere–Ocean Dynamics. *Academic Press,* 662 pp..

Gupta, A., Birner, T., Dörnbrack, A., & Polichtchouk, I. (2021), Importance of gravity wave forcing for springtime southern polar vortex breakdown as revealed by ERA5. *Geophys. Res. Lett., 48*, e2021GL092762. doi.org/10.1029/2021GL092762

Hersbach, H., Bell, B., Berrisford, P., Hirahara, S., Horanyi, A., Munoz-Sabater, J., Nicolas, J., Peubey, C., Radu, R., Schepers, D., Simmons, A., Soci, C., Abdalla, S., Abellan, X., Balsamo, G., Bechtold, P., Biavati, G., Bidlot, J., Bonavita, M., De Chiara, G., Dahlgren, P., Dee, D., Diamantakis, M., Dragani, R., Flemming, J., Forbes, R., Fuentes, M., Geer, A., Haimberger, L., Healy, S., Hogan, R. J., Hólm, E., Janiskova, M., Keeley, S., Laloyaux, P., Lopez, P., Lupu, C., Radnoti, G., de Rosnay, P., Rozum, I., Vamborg, F., Villaume, S., & Thepaut, J.-N. (2020), The ERA5 global reanalysis. *Q. J. Roy. Meteorol. Soc., 146*, 1999–2049. doi.org/10.1002/qj.3803

Hertzog, A., Boccara, G., Vincent, R., Vial, F., & Coquerez, P. (2008), Estimation of gravity-wave momentum fluxes and phase speeds from long-duration stratospheric balloon flights. 2. Results from the Vorcore campaign in Antarctica, *J. Atmos. Sci., 65*, 3056–3070.

Hólm, E., Forbes, R., Lang, S., Magnusson, L., & Malardel, S. (2016), New model cycle brings higher resolution. *ECMWF Newsletter, No. 147*, ECMWF, Reading, UK, 14–19.

ICAO (2001), Meteorological service for international air navigation. *Annex 3 to the Convention on International Civil Aviation, 14th ed. International Civil Aviation Organization Doc.*, 128 pp..

Johansson, S., Woiwode, W., Höpfner, M., Friedl-Vallon, F., Kleinert, A., Kretschmer, E., Latzko, T., Orphal, J., Preusse, P., Ungermann, J., Santee, M. L., Jurkat-Witschas, T., Marsing, A., Voigt, C., Giez, A., Krämer, M., Rolf, C., Zahn, A., Engel, A., Sinnhuber, B.-M., & Oelhaf, H. (2018), Airborne limb-imaging measurements of temperature, HNO3, O3, ClONO2, H2O and CFC-12 during the Arctic winter 2015/2016: characterization, in situ validation and comparison to Aura/MLS. *Atmos. Meas. Tech., 11*, 4737–4756, doi.org/10.5194/amt-11-4737-2018

Kaifler, B. and Kaifler, N.: A Compact Rayleigh Autonomous Lidar (CORAL) for the middle atmosphere, Atmos. Meas. Tech., 14, 1715–1732, https://doi.org/10.5194/amt-14-1715-2021, 2021.

Kennedy, P. J., & Shapiro, M. A. (1975), The energy budget in a clear air turbulence zone as observed by aircraft. *Mon. Wea. Rev., 103*, 650–654. doi.org/10.1175/1520-0493(1975)103,0650:TEBIAC.2.0.CO;2

Knox, J. A. (1997), Possible Mechanisms of Clear-Air Turbulence in Strongly Anticyclonic Flows. *Monthly Weather Review*, *125*(6), 1251-1259. doi.org/10.1175/1520-0493(1997)125<1251:PMOCAT>2.0.CO;2

Knox, J. A., McCann, D. W., & Williams, P. D. (2008), Application of the Lighthill–Ford Theory of Spontaneous Imbalance to Clear-Air Turbulence Forecasting. *Journal of the Atmospheric Sciences*, *65*(10), 3292-3304. doi.org/10.1175/2008JAS2477.1

Koch, S. E., Jamison, B. D., Lu, C. G., Smith, T. L., Tollerud, E. I., Girz, C., Wang, N., Lane, T. P., Shapiro, M. A., Parrish, D. D., & Cooper, O. R. (2005), Turbulence and gravity waves within an upper-level front. *J. Atmos. Sci., 62*, 3885–3908. doi.org/10.1175/Jas3574.1

Krasauskas, L., Ungermann, J., Preusse, P., Friedl-Vallon, F., Zahn, A., Ziereis, H., Rolf, C., Plöger, F., Konopka, P., Vogel, B., & Riese, M. (2021), 3-D tomographic observations of Rossby

878 wave breaking over the North Atlantic during the WISE aircraft campaign in 2017. *Atmos. Chem.*
879 *Phys., 21*, 10249–10272. doi.org/10.5194/acp-21-10249-2021

880 Krautstrunk, M., & Giez, A. (2012), The Transition from FALCON to HALO era airborne
881 atmospheric research. *in: Atmospheric Physics, edited by: Schumann, U., Research Topics in*
882 *Aerospace, Springer Verlag, Berlin*, 609–624. doi.org/10.1007/978-3-642-30183-4_37

883 Krisch, I., Preusse, P., Ungermann, J., Dörnbrack, A., Eckermann, S. D., Ern, M., Friedl-Vallon,
884 F., Kaufmann, M., Oelhaf, H., Rapp, M., Strube, C., & Riese, M. (2017), First tomographic
885 observations of gravity waves by the infrared limb imager GLORIA. *Atmos. Chem. Phys., 17*,
886 14937–14953. doi.org/10.5194/acp-17-14937-2017

887 Kruse, C. G., & Smith, R. B. (2015), Gravity Wave Diagnostics and Characteristics in Mesoscale
888 Fields. *Journal of the Atmospheric Sciences, 72*, 4372-4392. doi.org/10.1175/JAS-D-15-0079.1

889 Lim, E., Hendon, H. H., Butler, A. H., Thompson, D. W. J., Lawrence, Z. D., Scaife, A. A.,
890 Shepherd, T. G., Polichtchouk, I., Nakamura, H., Kobayashi, C., Comer, R., Coy, L., Dowdy, A.,
891 Garreaud, R. D., Newman, P. A., & Wang, G. (2021), The 2019 Southern Hemisphere
892 Stratospheric Polar Vortex Weakening and Its Impacts. *Bulletin of the American Meteorological*
893 *Society, 102*(6), E1150-E1171. https://doi.org/10.1175/BAMS-D-20-0112.1

894 Magnusson, L., Chen, J.-H., Lin, S.-J., Zhou, L., & Chen, X. (2019), Dependence on initial
895 conditions versus model formulations for medium-range forecast error variations. *Q J R Meteorol*
896 *Soc., 145*, 2085–2100. doi.org/10.1002/qj.3545

897 Malardel, S., & Wedi, N. P. (2016), How does subgrid-scale parametrization influence nonlinear
898 spectral energy fluxes in global NWP models? *J. Geophys. Res.-Atmos., 121*, 5395–5410.
899 doi.org/10.1002/2015JD023970

900 Mauritsen, T., & Svensson, G. (2007). Observations of Stably Stratified Shear-Driven
901 Atmospheric Turbulence at Low and High Richardson Numbers, Journal of the Atmospheric
902 Sciences, 64(2), 645-655. doi.org/10.1175/JAS3856.1

903 O'Sullivan, D., & Dunkerton, T. J. (1995), Generation of Inertia–Gravity Waves in a Simulated
904 Life Cycle of Baroclinic Instability, *Journal of Atmospheric Sciences*, *52*(21), 3695-3716.
905 doi.org/10.1175/1520-0469(1995)052<3695:GOIWIA>2.0.CO;2

906 Panofsky, H. A., Dutton, J. A., Hemmerich, K. H., McCreary, G., & Loving, N. V. (1969), Case
907 Studies of the Distribution of CAT in the Troposphere and Stratosphere. *Journal of Applied*
908 *Meteorology and Climatology*, *7* (3), 384–389. doi: 10.1175/1520-
909 0450(1968)007⟨0384:CSOTDO⟩2.0.CO;2

910 Plougonven, R., & Teitelbaum, H. (2003), Comparison of a large-scale inertia-gravity wave as
911 seen in the ECMWF analyses and from radiosondes. *Geophys. Res. Lett., 30*, 1954,
912 doi:10.1029/2003GL017716, 18.

Plougonven, R., Hertzog, A., & Guez, L. (2013), Gravity waves over Antarctica and the Southern Ocean: Consistent momentum fluxes in mesoscale simulations and stratospheric balloon observations. *Q. J. R. Meteorol. Soc., 139*, 101–118.

Plougonven, R., & Zhang, F. (2014), Internal gravity waves from atmospheric jets and fronts. *Rev. Geophys., 52*, 33–76. doi:10.1002/2012RG000419

Plougonven, R., & Zhang, F. (2016), Gravity waves generated by jets and fronts and their relevance for clear-air turbulence. *in: Aviation Turbulence, Springer International Publishing, Cham, Switzerland*, 385–406.

Rapp, M., Kaifler, B., Dörnbrack, A., Gisinger, S., Mixa, T., Reichert, R., Kaifler, N., Knobloch, S., Eckert, R., Wildmann, N., Giez, A., Krasauskas, L., Preusse, P., Geldenhuys, M., Riese, M., Woiwode, W., Friedl-Vallon, F., Sinnhuber, B., Torre, A. d. l., Alexander, P., Hormaechea, J. L., Janches, D., Garhammer, M., Chau, J. L., Conte, J. F., Hoor, P., & Engel, A. (2021), SOUTHTRAC-GW: An Airborne Field Campaign to Explore Gravity Wave Dynamics at the World's Strongest Hotspot. *Bulletin of the American Meteorological Society*, *102*(4), E871-E893. doi.org/10.1175/BAMS-D-20-0034.1

Riese, M., Oelhaf, H., Preusse, P., Blank, J., Ern, M., Friedl-Vallon, F., Fischer, H., Guggenmoser, T., Höpfner, M., Hoor, P., Kaufmann, M., Orphal, J., Plöger, F., Spang, R., Suminska-Ebersoldt, O., Ungermann, J., Vogel, B., & Woiwode, W. (2014), Gimballed Limb Observer for Radiance Imaging of the Atmosphere (GLORIA) scientific objectives. *Atmos. Meas. Tech., 7*, 1915–1928. doi.org/10.5194/amt-7-1915-2014

Rodriguez Imazio, P., Dörnbrack, A., Urzua, R. D., Rivaben, N., & Godoy, A. (2022). Clear Air Turbulence Observed Across a Tropopause Fold Over the Drake Passage - A Case Study. *Journal of Geophysical Research: Atmospheres*, 127(4), e2021JD035908. doi: https://doi.org/10.1029/2021JD035908

Shapiro, M. A. (1980), Turbulent Mixing within Tropopause Folds as a Mechanism for the Exchange of Chemical-Constituents between the Stratosphere and Troposphere. *J. Atmos. Sci., 37*, 994–1004.

Sharman, R. D., Trier, S. B., Lane, T. P., & Doyle, J. D. (2012), Sources and dynamics of turbulence in the upper troposphere and lower stratosphere: A review. *Geophys. Res. Lett., 39*, L12803. doi.org/10.1029/2012GL051996

Sharman, R. D., Cornman, L. B., Meymaris, G., Pearson, J., & Farrar, T. (2014), Description and Derived Climatologies of Automated In Situ Eddy-Dissipation-Rate Reports of Atmospheric Turbulence. *Journal of Applied Meteorology and Climatology*, *53*(6), 1416-1432. doi.org/10.1175/JAMC-D-13-0329.1

Smith, R. B., Woods, B. K., Jensen, J., Cooper, W. A., Doyle, J. D., Jiang, Q., & Grubišić, V. (2008), Mountain Waves Entering the Stratosphere. *Journal of the Atmospheric Sciences, 65*, 8, 2543-2562. doi.org/10.1175/2007JAS2598.1

Smith, R. B., Nugent, A. D., Kruse, C. G., Fritts, D. C., Doyle, J. D., Eckermann, S. D., Taylor, M. J., Dörnbrack, A., Uddstrom, M., Cooper, W., Romashkin, P., Jensen, J., & Beaton, S. (2016), Stratospheric Gravity Wave Fluxes and Scales during DEEPWAVE. *Journal of the Atmospheric Sciences, 73*, 7, 2851-2869. doi.org/10.1175/JAS-D-15-0324.1

Stein, A. F., Draxler, R. R., Rolph, G. D., Stunder, B. J. B., Cohen, M. D., & Ngan, F. (2015), NOAA's HYSPLIT Atmospheric Transport and Dispersion Modeling System. *B. Am. Meteorol. Soc., 96*, 2059–2077. doi.org/10.1175/BAMS-D-14-00110.1

Stenke, A., Grewe, V., & Ponater, M. (2008), Lagrangian transport of water vapour and cloud water in the ECHAM4 GCM and its impact on the cold bias. *Clim. Dynam., 31*, 491–506. doi.org/10.1007/s00382-007-0347-5

Strauss, L., Serafin, S., Haimov, S., & Grubii, V. (2015), Turbulence in breaking mountain waves and atmospheric rotors estimated from airborne in situ and Doppler radar measurements. *Quart. J. Roy. Meteor. Soc., 141*, 3207–3225. doi.org/10.1002/qj.2604

Ungermann, J., Blank, J., Lotz, J., Leppkes, K., Hoffmann, L., Guggenmoser, T., Kaufmann, M., Preusse, P., Naumann, U., & Riese, M. (2011), A 3-D tomographic retrieval approach with advection compensation for the air-borne limb-imager GLORIA. *Atmos. Meas. Tech., 4*, 2509–2529. doi.org/10.5194/amt-4-2509-2011

Ungermann, J., Kleinert, A., Maucher, G., Bartolomé, I., Friedl-Vallon, F., Johansson, S., Krasauskas, L., & Neubert, T. (2022), Quantification and mitigation of the instrument effects and uncertainties of the airborne limb imaging FTIR GLORIA. *Atmos. Meas. Tech., 15*, 2503–2530. doi.org/10.5194/amt-15-2503-2022

Vadas, S. L., & Fritts, D. C. (2001), Gravity Wave Radiation and Mean Responses to Local Body Forces in the Atmosphere. *Journal of the Atmospheric Sciences*, *58*(16), 2249-2279. doi.org/10.1175/1520-0469(2001)058<2249:GWRAMR>2.0.CO;2

Vadas, S. L., & Becker, E. (2018), Numerical modeling of the excitation, propagation, and dissipation of primary and secondary gravity waves during wintertime at McMurdo Station in the Antarctic. *Journal of Geophysical Research: Atmospheres, 123*, 9326– 9369. doi.org/10.1029/2017JD027974

Vadas, S. L., Zhao, J., Chu, X., & Becker, E. (2018). The excitation of secondary gravity waves from local body forces: Theory and observation. *Journal of Geophysical Research: Atmospheres, 123*, 9296– 9325. doi.org/10.1029/2017JD027970

Wei, J., & Zhang, F. (2014), Mesoscale Gravity Waves in Moist Baroclinic Jet–Front Systems. *Journal of the Atmospheric Sciences, 71*(3), 929-952. doi.org/10.1175/JAS-D-13-0171.1

Wetzel, G., Friedl-Vallon, F., Glatthor, N., Grooß, J.-U., Gulde, T., Höpfner, M., Johansson, S., Khosrawi, F., Kirner, O., Kleinert, A., Kretschmer, E., Maucher, G., Nordmeyer, H., Oelhaf, H., Orphal, J., Piesch, C., Sinnhuber, B.-M., Ungermann, J., & Vogel, B. (2021), Pollution trace gases C2H6, C2H2, HCOOH, and PAN in the North Atlantic UTLS: observations and simulations. *Atmos. Chem. Phys., 21*, 8213–8232. doi.org/10.5194/acp-21-8213-2021

988 Woiwode, W., Dörnbrack, A., Polichtchouk, I., Johansson, S., Harvey, B., Höpfner, M.,
989 Ungermann, J., & Friedl-Vallon, F. (2020), Technical note: Lowermost-stratosphere moist bias in
990 ECMWF IFS model diagnosed from airborne GLORIA observations during winter–spring 2016.
991 *Atmos. Chem. Phys., 20*, 15379–15387. doi.org/10.5194/acp-20-15379-2020

992